



# Chapter 5

## Neutron Induced Reaction Cross-sections

---

The chapter presents the measurement of neutron induced cross-sections of  $^{232}\text{Th}(n, \gamma)^1$ ,  $^{100}\text{Mo}(n, 2n)^2$ , and  $^{58}\text{Ni}(n, x)^3$  reactions using quasi - monoenergetic neutrons generated by  $^7\text{Li}(p, n)$  reaction. The present chapter also provides the theoretically calculated cross-section data for tin (Sn) isotopes<sup>4</sup> using TALYS and EMPIRE model codes up to 20 MeV neutron energies. The data for Sn isotopes were also calculated using different systematics. TALYS, ALICE, EMPIRE codes were used together with the ENDF/B-VII.1, JENDL-4.0, JEFF-3.2, and CENDL-3.1 evaluated data libraries to compare the present findings. The results of this chapter are important for advanced reactor/accelerator technology, dose estimation of different radioisotopes and nuclear medicine. The results also highlight that  $^7\text{Li}(p, n)$  reaction is suitable for the measurement of reaction cross-section data up to 20 MeV incident proton energies by applying the low-energy neutron correction.

---

### Publications Related to the Present Chapter...

- 
- |   |              |
|---|--------------|
| <sup>1</sup> S. Parashari, S. Mukherjee et al., <i>Phys. Rev. C</i> <b>98</b> (2018) 014625.    | I.F. = 3.132 |
| <sup>2</sup> S. Parashari, S. Mukherjee et al., <i>Phys. Rev. C</i> <b>99</b> (2019) 044602.    | I.F. = 3.132 |
| <sup>3</sup> S. Parashari, S. Mukherjee et al., <i>Eur. Phys. Jour. A</i> <b>55</b> (2019) 51.  | I.F. = 2.581 |
| <sup>4</sup> S. Parashari, S. Mukherjee et. al., <i>App. Rad. Iso.</i> <b>133</b> (2018) 31-37. | I.F. = 1.343 |

## 5.1 Introduction

Extensive work has been carried out over the years in order to make nuclear energy more efficient and to reduce the production of long-lived actinides. A solution is to convert long-lived radioisotopes into short-lived isotopes which can then be decayed to a safe radiation limit to be handled properly. Other solution is to use an alternative fuel which would produce efficient energy and a considerably less production of radioisotopes having a long half-life. ADSs<sup>5</sup> [1–8] may provide both the solutions together as it can be used in a reactor producing efficient green energy and on the other hand, it can also be used for the transmutation of long-lived isotopes into short ones [1–4]. Thorium (Th), available naturally with one isotope, is highly abundant in India [9]. The properties of an ADSs device makes it important for India's increasing energy demand [5–8] without effecting the environment. The present work is aimed specifically to measure the behavior of primary reaction channels of  $^{232}\text{Th}$  isotope at high incident neutron energies. To do so, the  $^{232}\text{Th}(n, \gamma)$  reaction cross-sections have been studied within the incident neutron energies 10-20 MeV. The effect of  $^{232}\text{Th}(n, 2n)$  reaction has also been studied [10].

A considerable amount of work has also been carried out to understand the behavior of different materials in extreme environment of a nuclear reactor. Different metals/alloys have different properties that make them suitable to be used in the structural components of a reactor, which are able to withstand the high radiation dose coming from a reactor core. Nickel (Ni) and molybdenum (Mo), being a refractory metal, are used in different reactor grade steel alloys [11] to make high strength materials. Both of the metals are also used in reactor structural materials. Ni is used in cladding steel alloys, like; Zircoloy-2 and Zircoloy-4 [11, 12], in which Ni and Fe has been reduced as the alloy produces hydrogen above a certain limit. The physical and chemical properties of both Ni and Mo makes them suitable to be used as structural material in ADSs and ITER [1, 13]. Therefore, the primary (n, x) reaction data are important for radiation damage, dose estimation and to predict the production of long/short-lived minor actinides within the surrounding materials of a reactor. On the other hand, the two isotopes are also important for nuclear medicine industry. Mo is used worldwide to produce  $^{99m}\text{Tc}$  isotope which is used in imaging and diagnostics [14, 15]. The  $^{99m}\text{Tc}$  is used for about 80% of imaging procedures like, single proton emission computed tomography (SPECT), bone and brain scans, myocardial perfusion imaging (MPI), etc. [14, 15]. The majority of the isotope is produced as a byproduct of spent reactor fuel, which effects the cost and

<sup>5</sup>A brief discussion on ADSs is provided in section 1.2

the availability of the medicine. Different reaction channels of Mo reaction with proton and neutron can be used to produce  $^{99m}\text{Tc}$  isotope for its instant uses [16–19]. The  $^{58}\text{Co}$  isotope produced by  $^{58}\text{Ni}(n, p)$  reaction is used as a trace element for the B12 vitamin absorption in human body [20].

In addition to ADSs, ITER<sup>6</sup> [13] is also being developed to produce even more efficient energy without producing any hazardous radiochemical waste. ITER can address the issue of waste disposal and energy requirement at once. The scattered radiation from an operational ITER may cause radiation damage to the surrounding materials, as already discussed in section 1.3. The toroidal coils of ITER holds the plasma inside the core, get the maximum irradiation from neutrons, high energy protons and  $\alpha$ -particles. The coils are made of  $\text{Nb}_3\text{Sn}$ , a superconducting material to make high magnetic field to hold the plasma inside the core [21]. Tin (sn) being used in the coils, becomes important to study for neutron reaction channels to estimate safety and secondary particle production rates.

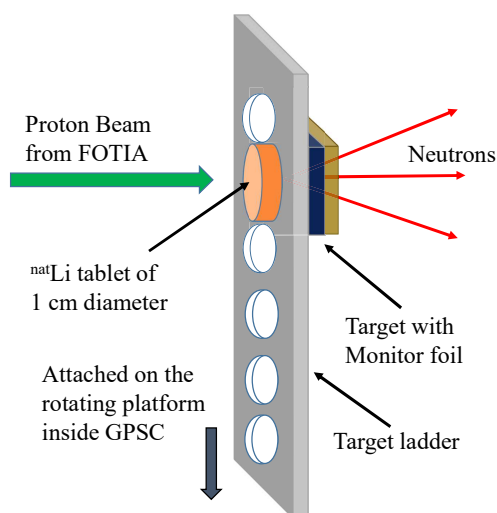


**Figure 5.1:** A schematic diagram of the target irradiation setup at BARC-FOTIA with  $^{nat}\text{LiF}$  tablet [23].

In view of the above, neutron induced reaction cross-sections were measured for  $^{232}\text{Th}$ , [10]  $^{100}\text{Mo}$ , [22] and  $^{58}\text{Ni}$  [23] by using quasi-monoenergetic neutrons produced by  $^{nat}\text{Li}(p, n)$  reaction for incident neutron energies up to 20 MeV. Off-line  $\gamma$ -ray spectroscopic method is used with neutron activation analysis of the produced residues to measure the cross-sections. Covariance analysis [24] is used to calculate the uncertainties in the measured data. Additionally, reaction cross-sections for different isotopes of Sn have been studied [25] theoretically by using TALYS [26] and EMPIRE [27]

<sup>6</sup>A brief summary about ITER devices is given in section 1.3

nuclear model codes. Different (n, p), (n, 2n), and (n,  $\alpha$ ) systematics [28–38] were also used to present a comparison among the calculated data. The present chapter first provides a detailed description of the neutron irradiation experiment with neutron flux measurement, corrections applied in flux calculations. Later, the calculations are provided for individual measurement and detailed discussion of the excitation functions.

**Table 5.1:** A summary of the experimental work carried out at BARC FOTIA accelerator facility

Experimental Details	Set 1
<i>Proton energies</i>	5 and 5.4
<i>neutron energies</i>	2.97 and 3.37
<i>Sample reactions</i>	$^{58}\text{Ni}(n, p)^{58}\text{Co}$
<i>Monitor reactions</i>	$^{197}\text{Au}(n, \gamma)^{198}\text{Au}$
<i>Sample thickness</i>	0.025 mm
<i>Monitor thickness</i>	0.025 mm
<i>Sample weight</i>	127.4 and 113.1 mg
<i>Monitor weight</i>	107 and 138.7 mg
<i>Sample dimensions</i>	$1.1 \times 1.2, 1.25 \times 0.75 \text{ cm}^2$
<i>Monitor dimensions</i>	$1.0 \times 0.4, 1.1 \times 0.7 \text{ cm}^2$

## 5.2 Experimental Details

The experiments for measurement of the neutron induced reaction cross-section of  $^{232}\text{Th}$  [10],  $^{100}\text{Mo}$  [22], and  $^{58}\text{Ni}$  [23] have been carried out at the BARC-TIFR Pelletron and BARC FOTIA<sup>7</sup> accelerators. Conventional neutron activation analysis<sup>8</sup> was adopted for the measurements. In the experiments performed at FOTIA, a natural lithium fluoride ( $^{nat}\text{LiF}$ ) tablet ( $\approx 5$  mm thick and 1 cm diameter) was pasted at the front (proton beam facing side) of the target ladder. A metal target (sample) together with the monitor foil wrapped in thin Al foils ( $\approx 0.015$  mm thick), separately, was pasted at adjacent back side of the target ladder. A schematic diagram of the irradiation setup is shown in Figure 5.1. The target ladder is then put at the center of the general purpose scattering chamber (GPSC) at the beam hall of FOTIA. Proton beams of 5 and 5.4 MeV energies were used for the irradiation of targets. In both the experiments, beam current was kept

<sup>7</sup>The details of the Pelletron and FOTIA accelerators are provided in sections 2.1.1 and 2.1.2

<sup>8</sup>see section 1.6

constant at about  $\approx 30$  nA. The irradiated samples were counted by using a HPGe detector after appropriate cooling to keep the radiation dose to safe limits. A list of the irradiated samples with the monitors used at FOTIA facility is provided in Table 5.1.

**Table 5.2:** A summary of the experimental work carried out at BARC-TIFR Pelletron accelerator facility

Experimental Details	Set 1	Set 2	set 3
Proton energies (MeV)	13, 16, 17, 21	13, 16, 19, 22	8, 16, 19
neutron energies (MeV)	10.95, 13.97, 14.98, 18.99	10.95, 13.97, 16.99, 20.00	5.99, 13.97, 16.99
Sample reactions	$^{232}\text{Th}(n, \gamma)$	$^{100}\text{Mo}(n, 2n)$	$^{58}\text{Ni}(n, p), (n, 2n)$
Monitor reactions	$^{232}\text{Th}(n, f)^{97}\text{Zr}$	$^{27}\text{Al}(n, \alpha)$	$^{115}\text{In}(n, n')$ & $^{27}\text{Al}(n, \alpha)$
Sample thickness	0.025 mm	0.1 mm	0.025 mm
Monitor thickness	0.025 mm	0.1 mm	0.1 mm (In & Al)
Sample weight	$\approx 211$ mg	$\approx 105$ mg	$\approx 22$ mg
Monitor weight	$\approx 211$ mg	$\approx 30$ mg	$\approx 140$ mg (In) & $\approx 30$ mg (Al)
Sample dimensions	$\approx 1 \times 0.5 \text{ cm}^2$	$1 \times 1 \text{ cm}^2$	$1 \times 1 \text{ cm}^2$
Monitor dimensions	$\approx 1 \times 0.5 \text{ cm}^2$	$1 \times 1 \text{ cm}^2$	$1 \times 1 \text{ cm}^2$

In the experiments performed at the BARC-TIFR Pelletron facility situated at Mumbai, India, a natural lithium target ( $^{nat}\text{Li}$ ) was used for the production of the neutron beams at different incident proton energies. A schematic diagram of irradiation facility at 6 meter port is shown in Figure 5.2. At the 6 meter port the irradiations were carried out inside a small chamber, in which the target (metal foils of specifically chosen targets) together with the monitor foils were either mounted on a tantalum based platform or can be put inside a small plastic pot just below the Ta platform. In the present case the Li foil encased in two Ta foils of varying thicknesses at front and back side, were mounted at on a platform with the help of screws. The Ta foils at both sides of the Li sophisticates the process of mounting the Li at 6 meter port. It also serves the purpose to completely stop the proton beam at thick Ta foil present at the back of the Li. The proton beam produces neutron beam of desired energy by the  $^7\text{Li}(p, n)$  reaction ( $E_{th} = 1.881$  MeV) [39]. The neutrons thus generated activate the samples which are being put below the Ta platform. A list of experiments performed at the BARC-TIFR Pelletron setup containing different target monitor combination, thicknesses of used Li foils, Ta foils used for the Ta-Li-Ta stack, and the energies of the produced neutron beams are given in Table 5.2. A complete description on the generation of neutrons from  $^{nat}\text{Li}(p, n)$  reaction is pro-

vided in the following section. The samples irradiated with the neutrons are then counted with the help of a common HPGe detector setup connected with a PC based  $\gamma$ -acquisition software<sup>9</sup>. The samples were counted at distance of 1 cm from the detector head to maintain the dead time of the detector system below 2%. The detector system was pre-calibrated with a standard  $^{152}\text{Eu}$  source [40] and the resolution of detector was measured as  $\approx 1.88$  keV for the 1.33 MeV  $\gamma$ -line of  $^{60}\text{Co}$ .

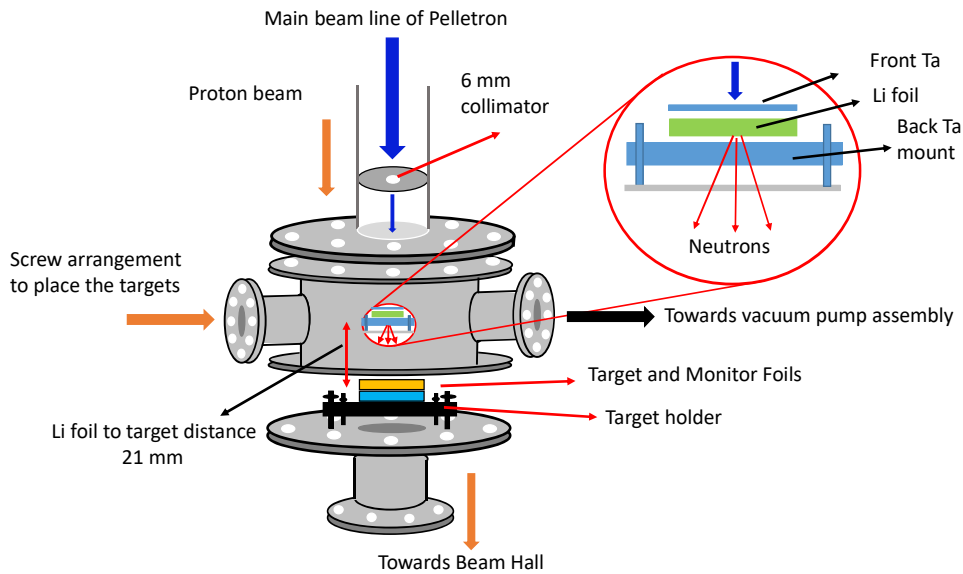


**Figure 5.2:** A schematic diagram of the target irradiation setup at BARC-TIFR Pelletron with  $^{nat}\text{Li}$  metal foil.

### 5.3 Measurement of Neutron Flux

Neutron beam was produced by using  $^{nat}\text{Li}(p, n)$  reaction. The interaction of high energy protons with a  $^{nat}\text{Li}$  target give rise to different nuclear reactions and many reaction channels take part and contribute in the outgoing neutron spectrum. Therefore, in general, the  $^{nat}\text{Li}(p, n)$  reaction remains a two-body reaction but higher energies quasi-monoenergetic neutron spectrum is produced, containing prominent peaks and a long continuum towards the lower neutron energies. The  $^7\text{Li}(p, n)^7\text{Be}$  reaction ( $E_{th} = 1.88$  MeV) [39] is the primary channel that contribute to the outgoing neutrons. The high energy group of neutrons produced by this reaction makes the prominent peak at the end point of the spectrum and known as the  $n_0$  group.

<sup>9</sup>see section 2.4.1

Secondly, the excited state of  ${}^7\text{Be}^*$  ( $E_{th} = 2.38$  MeV) [39] also populates and contribute to the spectrum via  $n_1$  group of neutrons. Since the thresholds for both the  $n_0$  and  $n_1$  groups fall within a few MeV region, therefore, the two groups reflect as a broad peak. As we increase the incident proton energy  $E_p \geq 2.4$  MeV, the  ${}^7\text{Li}(p, \gamma){}^8\text{Be}$  reaction ( $Q = -3.23$  MeV) [39] starts contributing. At energies  $E_p \geq 4.5$  MeV, the fragmentation of  ${}^8\text{Be}$  add up more low energy neutrons towards the tail region of the spectrum. At further higher energies, the breakup channels starts contributing and the neutron spectrum stretches into a continuum of low energy neutrons below 4 MeV incident proton energies.

The branching ratios of  $n_0$  and  $n_1$  group of neutrons up to 7 MeV were calculated by Liskien et al., [41] and Meadows et al., [42], Poppe et al., [43] calculated the extended branching ratios for both the ground and first excited state of  ${}^7\text{Be}$  up to 26 MeV. The parameterization of the neutron spectrum originating from the breakup channels is given by Meadows and Smith [42]. Using all the information given in the literature [41–46], the neutron spectra were generated for the desired energies. Scaling and interpolation was done wherever necessary to keep the threshold for all the neutron at  $E_p - 1.88$  MeV. The neutron spectrum for energies within 5-22 MeV are given in Figures 5.3. These neutron spectra have been used by different groups [47–49] for similar reaction cross-section studies.

The calculation for the neutron flux by using these distributions are straight forward. We fold the neutron spectrum with either the theoretical cross-sections from TALYS [26] or from the evaluated data libraries like ENDF/B-VII.1 [50]. The following equation is used for the calculation of the weighted average cross-section of the monitor reaction,

$$\langle \sigma_W \rangle = \frac{\sum_{E_i} \phi_i \sigma_i}{\sum_{E_i} \phi_i} \quad (5.1)$$

where,  $\sigma_W$  is the weighted average cross-section for the monitor reaction,  $\sigma_i$  is the monitor reaction cross-section and  $\phi_i$  is the neutron flux at energies  $E_i$ . The equation 5.1 is a discrete form of equation 3.18,

$$\langle \sigma_W \rangle = \frac{\int_{E_i} \phi_{E_i} \sigma_{E_i}}{\int_{E_i} \phi_{E_i}}. \quad (5.2)$$

The  $\sigma_W$  is now used in equation 3.17 to calculate the neutron flux for the particular irradiation. The final equation 3.19 is then used for the calculation of the reaction cross-section for a particular interaction.

**Table 5.3:** Nuclear spectroscopic data for the isotopes used in the measurement of the  $^{232}\text{Th}(n, \gamma)$ ,  $^{100}\text{Mo}(n, 2n)$  and  $^{58}\text{Ni}(n, x)$  reaction cross-sections. The data are taken from the NuDat [40], Q-value calculator and Q-tool [39] data library.

Reaction	Threshold (Q-value) (MeV)	$T_{1/2}$	Decay Mode (%)	$E_\gamma$ (keV)	$I_\gamma$ (%)
$^{232}\text{Th}(n, f)^{97}\text{Zr}(\text{m})$	—	$16.749 \pm 0.008$ h	$\beta^-$ (100)	743.36	$93.09 \pm 0.01$
$^{232}\text{Th}(n, \gamma)^{233}\text{Th}$	—(4.78)	$21.83 \pm 0.04$ min	$\beta^-$ (100)	-	-
$^{233}\text{Th} \xrightarrow{\beta^-} ^{233}\text{Pa}$	—	$26.975 \pm 0.013$ d	$\beta^-$ (100)	311.90	$38.5 \pm 0.4$
$^{27}\text{Al}(n, \alpha)^{24}\text{Na}(\text{m})$	3.249 (3.13)	$14.997 \pm 0.012$ h	$\beta^-$ (100%)	1368.68	$89.43 \pm 0.23$
$^{100}\text{Mo}(n, 2n)^{99}\text{Mo}$	8.37 (8.29)	$65.976 \pm 0.024$ h	$\beta^-$ (100%)	140.5	$9.9936 \pm 0.0015$
$^{197}\text{Au}(n, \gamma)^{198}\text{Au}(\text{m})$	— (0.65)	$2.6941 \pm 0.0002$ d	$\beta^-$ (100%)	411.8	95.62
$^{115}\text{In}(n, n')^{115\text{m}}\text{In}(\text{m})$	—	$4.486 \pm 0.004$ h	IT(95.00%) $\beta^-$ (5.00%)	336.2	$45.9 \pm 0.1$
$^{58}\text{Ni}(n, p)^{58}\text{Co}$	— (0.4)	$70.86 \pm 0.06$ d	$\epsilon$ (100%)	810.7	99.45
$^{58}\text{Ni}(n, 2n)^{57}\text{Ni}$	12.428 (12.21)	$35.60 \pm 0.06$ h	$\epsilon$ (100%)	1377.6	$81.70 \pm 0.24$

(m)  $\rightarrow$  monitor reaction, min  $\rightarrow$  minute, h  $\rightarrow$  hour, d  $\rightarrow$  day, y  $\rightarrow$  year

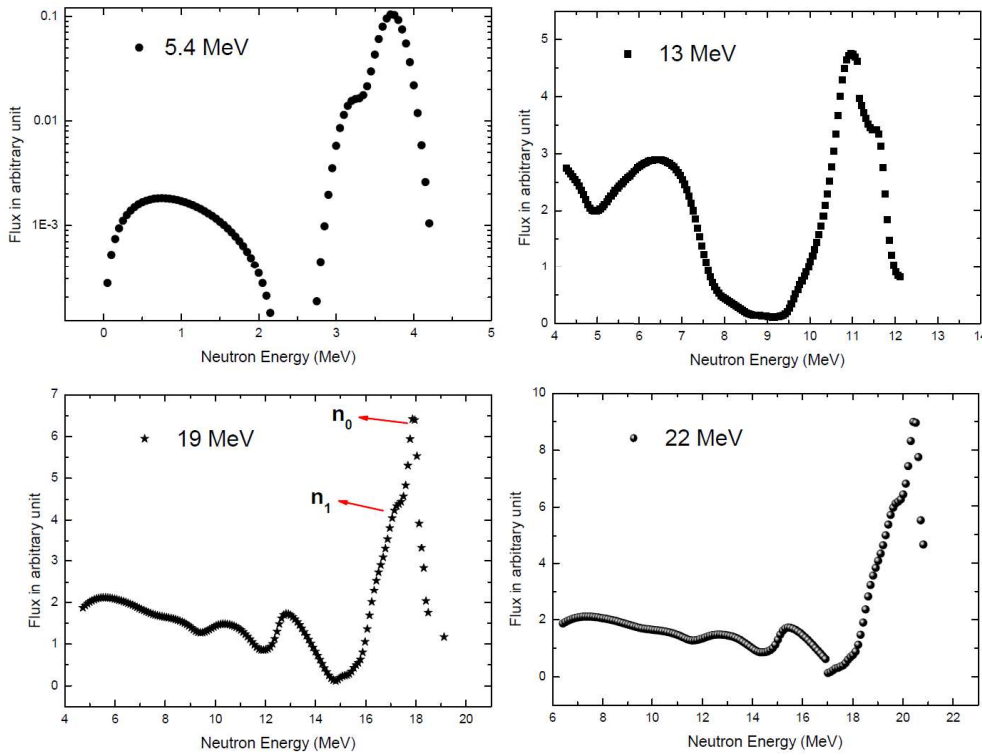


Figure 5.3: Typical neutron fluxes used for the present measurements reproduced by using the literature data and parameters given in Refs. [41–46].

## 5.4 Data Analysis for the $^{232}\text{Th}(n, \gamma)$ , $^{100}\text{Mo}(n, 2n)$ and $^{58}\text{Ni}(n, x)$ reactions

In the present work, the  $^{232}\text{Th}(n, \gamma)$  [10],  $^{100}\text{Mo}(n, 2n)$  [22],  $^{58}\text{Ni}(n, p)$ , and  $^{58}\text{Ni}(n, 2n)$  [23] reaction cross-section were measured within 3-20 MeV incident neutron energies. The proton beams of 5-22 MeV were used for the production of the neutrons of different energies using  $^7\text{Li}(p, n)$  neutron generator reaction. The neutron flux was measured by using the weighted average cross-sections from the chosen monitor reactions for specific targets. The cross-sections were measured by using the equation 3.19. The list of all the residues found to be populated in the neutron induced reactions with  $^{232}\text{Th}$ ,  $^{100}\text{Mo}$ , and  $^{58}\text{Ni}$  isotopes is given in Table 5.3. The typically recorded spectra for all the sample/monitor reactions are also given in the Figures 5.5, 5.6, and 5.7, respectively for Th, Mo and Ni isotopes.

The  $^{232}\text{Th}(n, \gamma)$  reaction cross-sections were measured from the delayed  $\gamma$ -lines of the  $^{233}\text{Pa}$  isotope. The flux for the reaction was measured by using the fission yield of the  $^{232}\text{Th}(n, f)^{97}\text{Zr}$  reaction. The  $^{97}\text{Zr}$  isotope decays with the  $\gamma$ -line of  $743.36 \pm 0.06$  keV ( $I_\gamma \rightarrow 93.09 \pm 0.01\%$ ) [40] having a half-life ( $T_{1/2}$ ) of  $16.749 \pm 0.008$  hours [40]. A typically recorded  $\gamma$ -spectrum for

the Th sample irradiated at 13.97 MeV neutron energy is shown in Figure 5.5. The total fission cross-section for the reaction were taken from the ENDF/B-VII.1 [50] data library. The experimental fission yield for  $^{97}\text{Zr}$  isotope at 14 MeV incident neutron energy was taken from the result by S. Mukherji et al., [55]. Similar yield datum was used by Shivashankar et al., [47] for the flux estimation by the  $^{232}\text{Th}(n, f)^{97}\text{Zr}$  reaction within the energy range of 5-20 MeV incident energies. Since the theoretical fission yield data remains almost constant around 14 MeV, therefore, it was assumed as constant for the energies under investigation. The flux estimated by using the weighted average cross-section of the  $^{232}\text{Th}(n, f)^{97}\text{Zr}$  reaction by using the equations 5.1 and 3.17 are given in Table 5.4. The  $(n, \gamma)$  reaction of  $^{232}\text{Th}$  results in the  $^{233}\text{Th}$  compound nucleus which undergo  $\beta^-$ -decay to  $^{233}\text{Pa}$ . The  $^{233}\text{Th}$  ( $T_{1/2} = 21.83 \pm 0.04$  min) compound nucleus formed in the prime interaction was allowed to decay before recording the spectrum for the  $^{233}\text{Pa}$  isotope activity. The daughter product  $^{233}\text{Pa}$  has a half-life ( $T_{1/2}$ ) of  $26.975 \pm 0.013$  days. The decaying  $\gamma$ -line of  $311.90 \pm 0.05$  keV ( $I_\gamma \rightarrow 38.5 \pm 0.4\%$ ) [40] was used for the calculations. The counting statistics were taken from the recorded spectra and the spectroscopic details for each calculation were taken from the NuDat [40] library, Q-Tool and Q-value calculator [39].

The  $^{100}\text{Mo}(n, 2n)^{99}\text{Mo}$  ( $E_{th} = 8.37$  MeV) [39] reaction cross-sections were measured relative to the  $^{27}\text{Al}(n, \alpha)^{24}\text{Na}$  ( $E_{th} = 3.249$  MeV) [39] monitor reaction cross-sections. A  $\gamma$ -line of 1368.68 keV ( $T_{1/2} \rightarrow 14.997 \pm 0.012$  hours,  $I_\gamma \rightarrow 99.9936 \pm 0.0015\%$ ) [40] was used for the flux estimation. A spectrum recorded for the monitor reaction at 13.97 MeV incident neutron energy is shown in Figure 5.6. The monitor cross-sections to be used in equation 5.1 for the weighted average cross-section were taken from the ENDF/B-VII.1 [50] data library. A correction is used in the neutron flux since the two reactions, monitor and sample, have different thresholds. The quasi-monoenergetic neutrons produced by  $^{nat}\text{Li}(p, n)$  reaction have a long tail part, from which the monitor reaction is sensitive up to 3.249 MeV. However, the sample reaction is only sensitive to the neutrons having energy 8.37 MeV or above. Therefore, the flux has been corrected to find the actual flux contributing to the sample reaction. This can be done by taking the area under the two threshold ranges as demonstrated in figure 5.4 with the ratio F as,

$$F = \frac{\text{Area under the curve from B to C}}{\text{Area under the curve from A to C}} \quad (5.3)$$

Now the actual flux can be obtained by multiplying the total flux with "F". A detailed description is also provided by R. Makwana et al., [46]. The final

#### 5.4. Data Analysis for the $^{232}\text{Th}(n, \gamma)$ , $^{100}\text{Mo}(n, 2n)$ and $^{58}\text{Ni}(n, x)$ reactions

values of the fluxes used for the cross-section measurement are given in Table 5.5. Similarly, the sample reaction cross-sections were calculated by using the counting statistics of the  $\gamma$ -line of 140.5 keV ( $T_{1/2} \rightarrow 65.976 \pm 0.024$  hours,  $I_\gamma \rightarrow 89.43 \pm 0.23\%$ ) [40]. A natural sample of Mo has been used for the present study, therefore, not only the  $^{100}\text{Mo}(n, 2n)$  contributes to the production of  $^{99}\text{Mo}$ , the  $^{98}\text{Mo}(n, \gamma)$  channel also produce the same isotope. The counting statistics, thus, contains the  $\gamma$ -ray counts coming from both the channel. This has been taken care with the method proposed by Smith et al., [56]. The counts from the  $^{98}\text{Mo}(n, \gamma)$  channel has been separated from the total counts by the following equation,

$$R = C_{obs(n,2n)} / C_{obs(n,\gamma)} = \frac{a_{(100)}\sigma(n, 2n)}{a_{(98)}\sigma(n, \gamma)} \quad (5.4)$$

where,  $a_{(100)}$  and  $a_{(98)}$  are the isotopic abundances and  $\sigma_{n,2n}$  and  $\sigma_{(n,\gamma)}$  are the cross-sections calculated using TALYS-1.9 [26] model code, of  $^{100}\text{Mo}$  and  $^{98}\text{Mo}$ , respectively. The delineated counts of  $^{100}\text{Mo}(n, 2n)$  reaction then used in equation 3.19 to calculate the cross-sections.

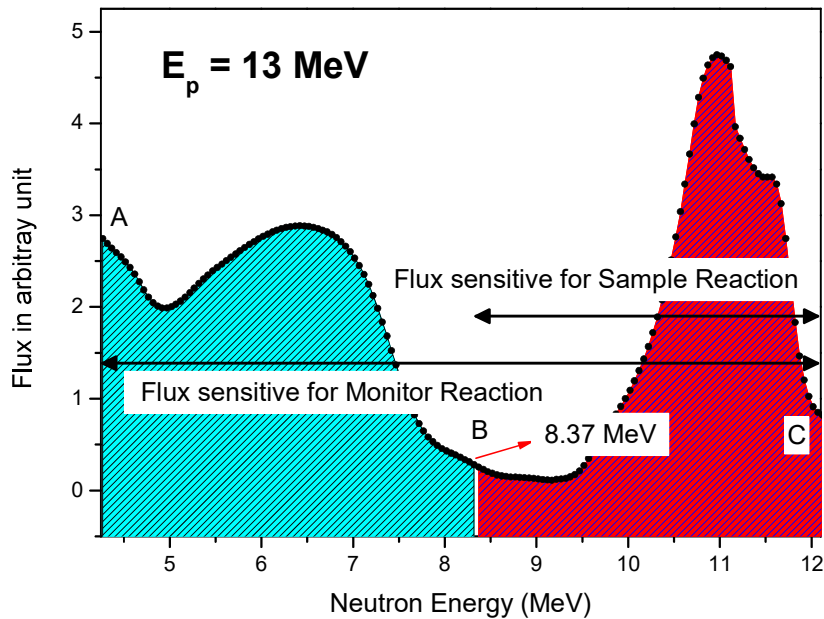


**Figure 5.4:** Demonstration of the neutron flux correction applied when the monitor and sample reactions have different thresholds [46].

The excitation function for  $^{58}\text{Ni}(n, x)$  reactions were measured by the neutron flux calculated by using a set of monitor reactions depending upon the reaction channel threshold [23]. The sample-monitor combinations

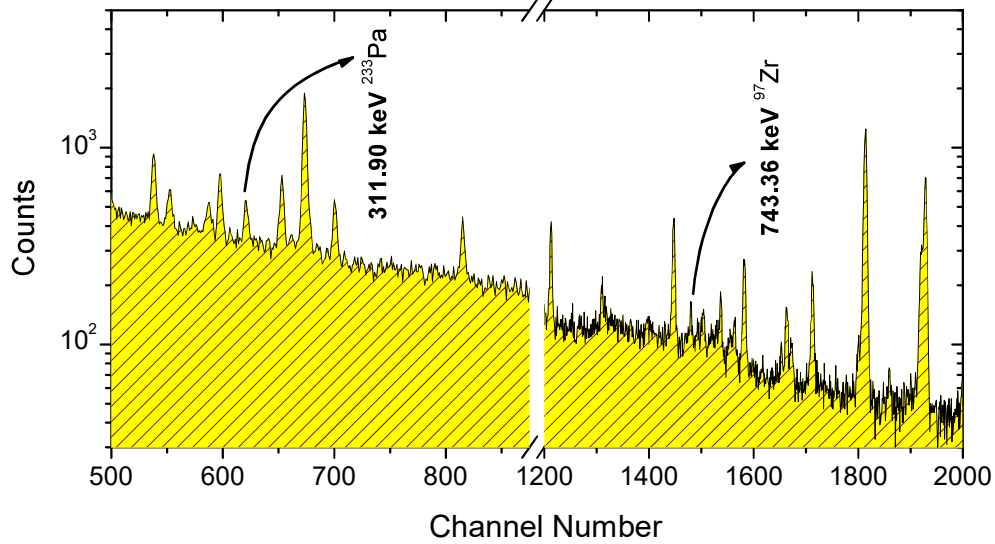


**Figure 5.5:** Typically recorded spectrum for the  $^{232}\text{Th}(n, f)$  monitor and  $^{232}\text{Th}(n, \gamma)$  sample reaction at 16 MeV incident proton energies [10].

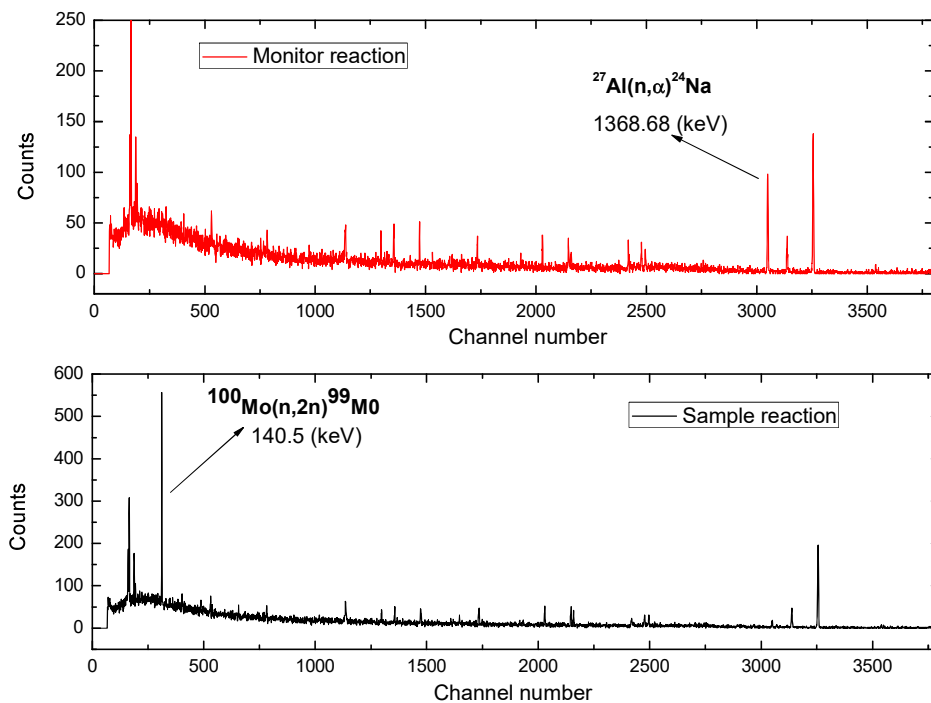


**Figure 5.6:** Typically recorded spectrum for the  $^{27}\text{Al}(n, \alpha)$  monitor and  $^{100}\text{Mo}(n, 2n)$  sample reaction at 19 MeV incident proton energies [22].

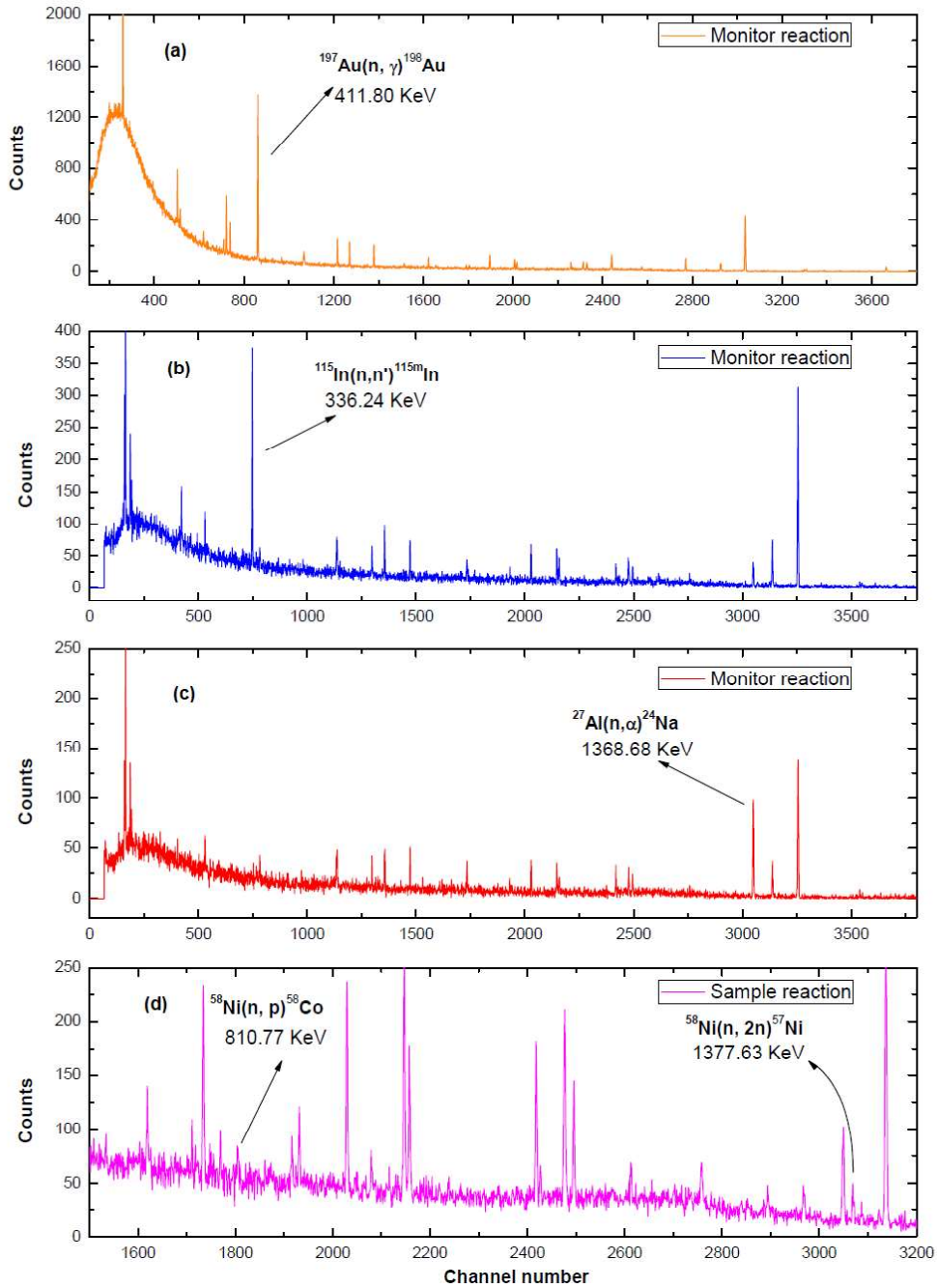


**Figure 5.7:** The typical recorded spectra for (a)  $^{197}\text{Au}(n, \gamma)$ , (b)  $^{115}\text{In}(n, n')$ , (c)  $^{27}\text{Al}(n, \alpha)$ , and (d)  $^{58}\text{Ni}(n, x)$  reactions at 19 MeV incident proton energy [23].

are also listed in Table 2.1. The  $^{197}\text{Au}(n, \gamma)$  reaction was used as monitor for  $^{58}\text{Ni}(n, p)$  reaction at 5 and 5.4 MeV incident proton energies. The  $^{115}\text{In}(n, n')$  reaction is used for  $^{58}\text{Ni}(n, p)$  reaction at energies 8, 16, and 19 MeV and the  $^{27}\text{Al}(n, \alpha)$  reaction is used for the  $^{58}\text{Ni}(n, 2n)$  reaction at 16 and 19 MeV. The primary  $\gamma$ -lines of all the monitor reactions were used for the flux calculations. A list of  $\gamma$ -rays used is given in the Table 5.3.

Typical recorded spectrum for all the monitor reactions  $^{197}\text{Au}(n, \gamma)^{198}\text{Au}$ ,  $^{115}\text{In}(n, n')^{115m}\text{In}$ , and  $^{27}\text{Al}(n, \alpha)^{24}\text{Na}$  are given in Figure 5.7(a)-(c). The monitor and sample reaction combination in case of  $^{58}\text{Ni}$  target were chosen according to the threshold of reactions under consideration. The evaluated data library ENDF/B-VII.1 [50] was used to find the weighted average cross-section of  $^{197}\text{Au}(n, \gamma)$  and  $^{27}\text{Al}(n, \alpha)$  reactions, however, EXFOR [57] experimental data was used to calculate the  $\langle \sigma_W \rangle$  for  $^{115}\text{In}(n, n')$  monitor reaction. The reason is, the data from the TALYS-1.9 [26], ENDF/B-VII.1 [50] or any other data library was found to be 10 times greater than the experimentally measured data for  $^{115}\text{In}(n, n')$  reaction. Also, flux from both the  $^{115}\text{In}(n, n')$  and  $^{27}\text{Al}(n, \alpha)$  reactions should match as they both get irradiated together. The neutron fluxes from both the reactions matches only when we use EXFOR data for  $^{115}\text{In}(n, n')$  reaction. The spectrum recorded for the sample reaction is shown in Figure 5.7(d). The counting statistics of the  $\gamma$ -lines of 810.77 keV ( $T_{1/2} \rightarrow 70.86 \pm 0.06$  days,  $I_\gamma \rightarrow 99.45\%$ ) and 1377.63 keV ( $T_{1/2} \rightarrow 35.60 \pm 0.06$  hours,  $I_\gamma \rightarrow 81.70 \pm 0.24\%$ ) [40] for both the  $^{58}\text{Ni}(n, p)^{58}\text{Co}$  and  $^{58}\text{Ni}(n, 2n)^{57}\text{Ni}$ , respectively, were used for cross-section measurements. The neutron flux correction, as mentioned for the  $^{100}\text{Mo}(n, 2n)$  reaction above<sup>10</sup>, is also applied in case of the  $^{58}\text{Ni}(n, 2n)$  reaction as the two reactions have a different thresholds (3.249 MeV for  $^{27}\text{Al}(n, \alpha)$  and 12.428 MeV for  $^{58}\text{Ni}(n, 2n)$  reaction).

The cross-section for each individual isotope produced in the interaction of neutrons with the selected targets was measured by using the standard NAA equation 3.19 as given below,

$$\sigma_R = \frac{C_{obs}\lambda(T_R/T_L)}{N_0 \langle \Phi \rangle \varepsilon_G I_\gamma K [1 - e^{-\lambda t_i}] [e^{-\lambda t_c}] [1 - e^{-\lambda T_L}]} \quad (5.5)$$

where the symbols have their usual meanings as described in section 3.1. A detailed discussion for each reaction is provided in the following sections. The uncertainties in the neutron induced reaction cross-sections were measured by using the covariance technique<sup>11</sup>, the results of which are given in Appendix A 7.3 for respective reaction.

<sup>10</sup>Described in Figure 5.4.

<sup>11</sup>A detailed discussion of the technique is given in section 3.2.

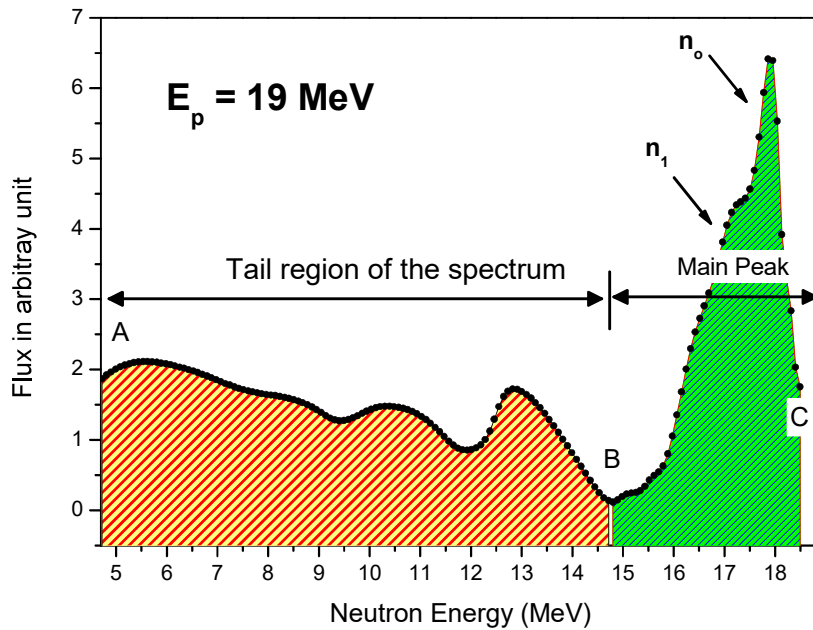


**Figure 5.8:** Demonstration of the neutron tailing correction applied to remove the contribution coming from the low energy neutron continuum from the measured data.

## 5.5 Measurement of Reaction Cross-section and Correction due to the Contribution of Neutron Tail

As the neutron flux has been estimated by using the weighted average cross-section for each neutron distribution for respective irradiation, the reaction cross-sections were calculated first for the entire range of the neutrons present in the energy spectrum given in Figure 5.3. The measured cross-section, thus, consist of the contribution from the main peak ( $n_0$  and  $n_1$  neutrons) and a contribution from the tail part of the spectrum [10,16,22,46]. The contributing from the tail part is separated by taking weighted average cross-section for the neutron spectrum from A to B as shown in Figure 5.8. The tailing part cross-section is then subtracted from the total cross-section by using the equation,

$$\sigma_R = \frac{(\Sigma\phi\sigma)_{\text{from A to C}} - (\Sigma\phi\sigma)_{\text{from A to B}}}{(\Sigma\phi)_{\text{from A to C}}} \quad (5.6)$$

where, the first term on the numerator corresponds to the measured cross-section, second term gives the tailing part and the denominator is the

integrated flux over the entire range of spectrum. Evaluated cross-section data libraries ENDF/B-VII.1 [50], JENDL-4.0 [51] were used to calculate the second term in equation 5.6.

The results for the  $^{232}\text{Th}(n, \gamma)^{233}\text{Pa}$  [10],  $^{100}\text{Mo}(n, 2n)^{99}\text{Mo}$  [22],  $^{58}\text{Ni}(n, p)^{58}\text{Co}$ , and  $^{58}\text{Ni}(n, 2n)^{57}\text{Ni}$  [23] reactions are provided in Tables 5.4, 5.5, 5.6, and 5.7, respectively. This method has been adopted in all the cases of neutron-induced reactions in the present work, as well as, by various authors [46–49,55] in recent years to find the correct value of the measured data. The uncertainties in the measured cross-section following the above mentioned technique requires a detailed survey including the errors from the monitor reaction and errors present in other quantities, which were used for the calculations at different steps. Also, the  $\gamma$ -ray spectroscopy was carried out by using a common setup, therefore, the data is correlated among different measured quantities. The covariance analysis [24], by using ratio method [24,47]<sup>12</sup>, was used to estimate the true errors and correlations exist in the measured data. Outcomes of the covariance analysis are presented in the following subsection for each reaction and the calculations from the first principal are shown in Appendix-A.

**Table 5.4:** Tailing corrected cross sections for  $^{232}\text{Th}(n, \gamma)^{233}\text{Th}$  reaction [10]

Neutron Energy (MeV)	Flux ( $n\text{ cm}^{-2}\text{s}^{-1}$ )	Cross-Section (mb)
$10.95 \pm 0.59$	$5.65 \times 10^6$	1.787
$13.97 \pm 0.57$	$2.35 \times 10^6$	1.207
$14.98 \pm 0.55$	$1.64 \times 10^6$	1.22
$18.99 \pm 0.65$	$8.49 \times 10^6$	0.529

**Table 5.5:** Tailing corrected cross sections for  $^{100}\text{Mo}(n, 2n)^{99}\text{Mo}$  reaction [22]

Neutron Energy (MeV)	Flux ( $n\text{ cm}^{-2}\text{s}^{-1}$ )	Cross-Section (mb)
$10.95 \pm 0.45$	$7.27 \times 10^5$	1243.89
$13.97 \pm 0.68$	$1.48 \times 10^6$	1422.53
$16.99 \pm 0.53$	$2.68 \times 10^6$	1216.82
$20.00 \pm 0.58$	$3.09 \times 10^6$	774.96

<sup>12</sup>See section 3.2

**Table 5.6:** Tailing corrected cross sections for  $^{58}\text{Ni}(n, p)^{58}\text{Co}$  reaction [23]

Neutron Energy (MeV)	Flux ( $n\text{ cm}^{-2}\text{s}^{-1}$ )	Cross-Section (mb)
$2.97 \pm 0.19$	$3.5 \times 10^6$	198.07
$3.37 \pm 0.23$	$3.8 \times 10^6$	252.21
$5.99 \pm 0.48$	$2.4 \times 10^6$	547.32
$13.97 \pm 0.68$	$3.2 \times 10^6$	421.29
$16.99 \pm 0.53$	$6.05 \times 10^6$	178.47

**Table 5.7:** Tailing corrected cross sections for  $^{58}\text{Ni}(n, 2n)^{57}\text{Ni}$  reaction [23]

Neutron Energy (MeV)	Flux ( $n\text{ cm}^{-2}\text{s}^{-1}$ )	Cross-Section (mb)
$13.97 \pm 0.68$	$1.48 \times 10^6$	31.28
$16.99 \pm 0.53$	$2.68 \times 10^6$	65.67

## 5.6 Covariance Analysis

In order to propagate the error from each parameter used in the calculation of the reaction cross-sections, error propagation<sup>13</sup> technique was utilized [24, 47]. In this technique, cross-section measurements have been carried out relative to a monitor reaction. The ratio method [24] provides the sophistication of including the uncertainties from each attribute into the final value. The covariance analysis was performed in each case, however, for reader's interest and clarity of the subject, detailed calculations are given below only for the  $^{232}\text{Th}(n, \gamma)^{233}\text{Th}$  reaction. For rest of the two cases,  $^{100}\text{Mo}(n, 2n)^{99}\text{Mo}$  and  $^{58}\text{Ni}(n, x)$  reactions, the detailed calculations are provided in Appendix A. In this method, first the covariance matrix is calculated by following the method given in the section 3.2.2. The list of the  $\gamma$ -lines and the corresponding measured efficiencies used in the present work are given in Table 5.8. The partial uncertainties in the four attributes,  $C$ ,  $I_\gamma$ ,  $N_0$ , and  $T_{1/2}$ , were first calculated using partial differentiation of equation 3.41, for the terms on the R.H.S. of the equation 3.43 for the 121.8

<sup>13</sup>The details regarding the covariance analysis are provided in section 3.2 of Chapter 3.

**Table 5.8:** Counting and spectroscopic details of the  $^{152}\text{Eu}$  source used for the efficiency measurement

Energy (keV)	Counts	$I_\gamma$ (%)	$N_0$	$T_{1/2}$ (years)	Efficiency
121.8	$2609402 \pm 2544$	$28.53 \pm 0.16$			0.51298464
244	$389703 \pm 948$	$7.55 \pm 0.04$			0.29692696
344	$1091614 \pm 1265$	$26.59 \pm 0.2$			0.2233512
411	$57237 \pm 368$	$2.237 \pm 0.013$			0.1527036
778.9	$225703 \pm 769$	$12.93 \pm 0.08$	$7800 \pm$	$13.517 \pm$	0.09754904
867	$64482 \pm 664$	$4.23 \pm 0.03$	$88.3^{(a)}$	$0.009^{(a)}$	0.089397
964	$214646 \pm 659$	$14.51 \pm 0.07$			0.07893738
1112	$180941 \pm 590$	$13.67 \pm 0.08$			0.069003
1212	$14101 \pm 231$	$1.633 \pm 0.011$			0.05858608
1299	$16650 \pm 217$	$1.415 \pm 0.008$			0.05742218
1408	$222960 \pm 523$	$20.87 \pm 0.09$			0.0560352

<sup>(a)</sup>Common for all the  $\gamma$ -lines

keV  $\gamma$ -line of  $^{152}\text{Eu}$  source<sup>14</sup> as,

$$\frac{\partial \epsilon}{\partial C} = \frac{1}{N_0 I_\gamma e^{-\lambda T} \Delta t} \quad (5.7)$$

multiply and divide the above equation by C,

$$\frac{\partial \epsilon}{\partial C} = \frac{1}{N_0 I_\gamma e^{-\lambda T} \Delta t} \left( \frac{C}{C} \right) \quad (5.8)$$

the first term in the above equation can be written as  $\epsilon$  and the equation can be rearranged for the infinitesimal variance as,

$$\Delta \epsilon = \frac{\epsilon}{C} \Delta C \quad (5.9)$$

where,  $\Delta \epsilon$  and  $\Delta C$  are the uncertainties in the efficiency and the counting statistics of the  $\gamma$ -line under consideration. Now  $\Delta \epsilon$  can be calculated as,

$$\Delta \epsilon = \frac{\epsilon}{C} \Delta C = \frac{0.51298464}{2609402} \times 2544 = 0.500127 \times 10^{-3} \quad (5.10)$$

similarly, the partial uncertainties due to  $I_\gamma$ ,  $N_0$ , and  $T_{1/2}$ , by omitting the negative sign can be calculated and are given in Table 5.9. The total uncertainty in the efficiency now can be calculated as the quadratic sum of

<sup>14</sup>The standard  $^{152}\text{Eu}$   $\gamma$ -ray source was used for the calibration efficiency measurement of the HPGe detector.

all the individual partial uncertainties from the four attributes, by following the equation 3.45 and also given in Table 5.9.

**Table 5.9:** Partial uncertainties in the efficiency

Energy (keV)	Partial uncertainty ( $\times 10^3$ ) due to attributes				Total uncertainty ( $\sigma_{\epsilon_{ij}} \times 10^3$ )
	$r = 1(C)$	$r = 2(I_\gamma)$	$r = 3(N_0)$	$r = 4(T_{1/2})$	
121.8	0.500127	2.876885	5.807249	0.017511	6.500081
244	0.722310	1.573122	3.361365	0.010135	3.780916
344	0.258827	1.679963	2.528450	0.007624	3.046701
411	0.981793	0.887414	1.728683	0.005212	2.177107
778.9	0.332362	0.603551	1.104305	0.003329	1.301629
867	0.920560	0.634021	1.012019	0.003051	1.507849
964	0.242351	0.380814	0.893612	0.002694	1.001150
112	0.225001	0.403821	0.781149	0.002355	0.907687
1212	0.959746	0.394639	0.663224	0.001999	1.231553
1299	0.748385	0.324648	0.650048	0.001961	1.043093
1408	0.131442	0.241646	0.634347	0.001912	0.691426

The calculated partial uncertainties from each attribute now be used in the equation 3.48, following the  $S_{ijr}$  matrices<sup>15</sup> for correlated and uncorrelated attributes, to calculate the covariance matrix for the efficiencies of the detector. The matrices thus formed for each attribute are then summed up in order to form a covariance matrix given in Table 5.10. Since the upper covariance matrices are the symmetric matrices, therefore, only the lower triangle of the matrix is shown in Table 5.10. The errors in the efficiency of the respective  $\gamma$ -line can be calculated by taking the square root of the diagonal elements of the matrix 5.10. The correlation coefficients among the efficiencies from different  $\gamma$ -lines can be obtained from non-diagonal elements using following equation and are given in Table 5.11.

$$Corr(\epsilon_{ij}) = \frac{V_{\epsilon_{ij}}}{\sqrt{V_{\epsilon_{ii}}} \times \sqrt{V_{\epsilon_{jj}}}} \quad (5.11)$$

Since the efficiencies used for the detector calibration are different from those used in the measurement of the reaction cross-sections, therefore, a linear model has been used to estimate the efficiencies and the relative uncertainties/correlations for the  $\gamma$ -lines used for, say, the  $^{232}\text{Th}(n, \gamma)$  reaction

<sup>15</sup>The definitions of  $S_{ijr}$  matrices for correlated, uncorrelated and partially correlated cases are given in subsection 3.2.2.

**Table 5.10:** Co-variance matrix ( $V_\epsilon \times 10^5$ ) for the detector efficiencies

4.225											
1.952	1.43										
1.468	0.85	0.928									
1.004	0.581	0.437	0.474								
0.641	0.371	0.279	0.191	0.169							
0.588	0.34	0.256	0.175	0.112	0.227						
0.519	0.3	0.226	0.154	0.099	0.09	0.1					
0.454	0.26	0.196	0.135	0.086	0.079	0.07	0.082				
0.385	0.223	0.168	0.115	0.073	0.067	0.059	0.052	0.152			
0.378	0.219	0.164	0.112	0.072	0.066	0.058	0.051	0.043	0.12		
0.368	0.213	0.160	0.11	0.07	0.064	0.057	0.05	0.042	0.041	0.048	

**Table 5.11:** Correlation matrix for for the detector efficiencies

1											
0.79	1										
0.74	0.73	1									
0.70	0.70	0.65	1								
0.75	0.75	0.70	0.67	1							
0.59	0.59	0.55	0.53	0.56	1						
0.79	0.79	0.74	0.71	0.75	0.60	1					
0.76	0.76	0.71	0.68	0.73	0.58	0.76	1				
0.48	0.47	0.44	0.42	0.45	0.36	0.48	0.46	1			
0.55	0.55	0.51	0.49	0.528	0.42	0.55	0.53	0.33	1		
0.81	0.82	0.76	0.73	0.78	0.62	0.82	0.78	0.49	0.57	1	

cross-section measurement. The complete method has been described in the subsection 3.2.2, to find out the covariance/correlation matrix for the desired efficiencies. The Table 5.12 shows the covariance and correlation matrix together with the measured uncertainties in the efficiencies for the  $\gamma$ -lines of sample and monitor reactions by using equations 3.49-3.54.

**Table 5.12:** Measured efficiencies with correlation matrix

$E_\gamma$ (keV)	Covariance Matrix ( $\times 10^6$ )	Correlation Matrix	Efficiency
311.90	7.75724	1	$0.229286 \pm 0.002785$
743.36	3.01161	0.904	$0.098438 \pm 0.001195$

Using the efficiencies and the correlations in the Table 5.12, the error

analysis for the cross-sections can now be performed along with considering the fractional uncertainties provided in the Table 5.13. The ratio method [24] has been discussed in section 3.2.3 in order to perform the calculations for the uncertainty analysis of the measured cross-sections relative to monitor data. The  $S_{ijr}$  matrices were used according to the correlation assigned at the bottom of the Table 5.13. The partial uncertainties in table 5.13 were calculated by differentiating the equation 3.57 partially, with respect to each parameter considered for the analysis. A sample calculation for the matrix  $(V_\sigma)_{ij}$  by taking counts ( $C_r$ ) and  $\gamma$ -ray intensities ( $I_{\gamma_r}$ ) for target reaction as the attribute is shown below,

**Table 5.13:** Fractional uncertainties in various parameters to obtain  $^{232}\text{Th}(n, \gamma)$  cross-section

$E_n$ (MeV)	Partial uncertainty (%)								
	$C_r$	$C_m$	$I_{\gamma_r}$	$I_{\gamma_m}$	$\eta_{r,x}$	$f_{\lambda_r}$	$f_{\lambda_m}$	$Y_f$	$\sigma_W$
10.95	10.755	17.803	1.038	0.0174	0.414	0.0421	0.0443	4.117	1.599
13.97	6.135	7.862	1.038	0.0174	0.414	0.0421	0.0443	4.117	1.603
14.98	6.623	19.277	1.038	0.0174	0.414	0.0421	0.0443	4.117	1.701
18.99	8.496	12.933	1.038	0.0174	0.414	0.0421	0.0443	4.117	1.698
Corr	0	0	1	1	1	1	1	1	0

$$\begin{aligned}
(V_\sigma)_{Counts} &= \begin{pmatrix} 0.1095 & 0 & 0 & 0 \\ 0 & 0.06135 & 0 & 0 \\ 0 & 0 & 0.06623 & 0 \\ 0 & 0 & 0 & 0.08496 \end{pmatrix} \times \begin{pmatrix} 1 & 0 & 0 & 0 \\ 0 & 1 & 0 & 0 \\ 0 & 0 & 1 & 0 \\ 0 & 0 & 0 & 1 \end{pmatrix} \\
&\times \begin{pmatrix} 10.95 & 0 & 0 & 0 \\ 0 & 6.135 & 0 & 0 \\ 0 & 0 & 6.623 & 0 \\ 0 & 0 & 0 & 8.496 \end{pmatrix} = \begin{pmatrix} \mathbf{0.01156} & \mathbf{0} & \mathbf{0} & \mathbf{0} \\ \mathbf{0} & \mathbf{0.00376} & \mathbf{0} & \mathbf{0} \\ \mathbf{0} & \mathbf{0} & \mathbf{0.00438} & \mathbf{0} \\ \mathbf{0} & \mathbf{0} & \mathbf{0} & \mathbf{0.00722} \end{pmatrix} \\
(V_\sigma)_{I_{\gamma_r}} &= \begin{pmatrix} 0.01038 & 0 & 0 & 0 \\ 0 & 0.01038 & 0 & 0 \\ 0 & 0 & 0.01038 & 0 \\ 0 & 0 & 0 & 0.01038 \end{pmatrix} \times \begin{pmatrix} 1 & 1 & 1 & 1 \\ 1 & 1 & 1 & 1 \\ 1 & 1 & 1 & 1 \\ 1 & 1 & 1 & 1 \end{pmatrix} \\
&\times \begin{pmatrix} 0.01038 & 0 & 0 & 0 \\ 0 & 0.01038 & 0 & 0 \\ 0 & 0 & 0.01038 & 0 \\ 0 & 0 & 0 & 0.01038 \end{pmatrix} = 0.0001079 \begin{pmatrix} \mathbf{1} & \mathbf{1} & \mathbf{1} & \mathbf{1} \\ \mathbf{1} & \mathbf{1} & \mathbf{1} & \mathbf{1} \\ \mathbf{1} & \mathbf{1} & \mathbf{1} & \mathbf{1} \\ \mathbf{1} & \mathbf{1} & \mathbf{1} & \mathbf{1} \end{pmatrix}
\end{aligned}$$

The matrices for rest of the attributes can be calculated as shown above and then added to form a final covariance matrix along with the correlation coefficients, given in Table 5.14. The error present in each measured cross-section is now can be calculated by taking the square root of the diagonal elements of the covariance matrix. The quantities at the diagonal are presented in (%), therefore, first they must be converted into their absolute value then the square root of the quantity will give the uncertainty present in the respective cross-section value. The Table 5.15 present the tailing corrected cross-section with the uncertainties calculated by using the error analysis, compared with the evaluated data libraries like; ENDF/B-VII.1 [50], JENDL-4.0 [51] and the theoretical data from TALYS [26].

**Table 5.14:** Covariance matrix (%) and corresponding correlation coefficients for the measured  $^{232}\text{Th}(n, \gamma)$  cross-sections

$E_n$ (MeV)	Covariance matrix ( $V_{cs_{ij}}$ )(%)				Correlation matrix			
10.95	4.5342				1			
13.97	0.1821	1.20234			0.078	1		
14.98	0.1821	0.1821	4.3657		0.041	0.079	1	
18.99	0.1821	0.1821	0.1821	2.6055	0.053	0.102	0.054	1

**Table 5.15:**  $^{232}\text{Th}(n, \gamma)$  reaction cross-sections at different neutron energies compare with ENDF-B/VII.1, JENDL-4.0 and TALYS-1.8 data

Neutron Energy (MeV)	Flux $n \text{ cm}^{-2} \text{ s}^{-1}$	Cross-Section (mb)			
		Corrected	ENDF-B/VII.1	JENDL-4.0	TALYS
$10.95 \pm 0.59$	$5.65 \times 10^6$	$1.787 \pm 0.378$	1.180	1.495	1.174
$13.97 \pm 0.57$	$2.35 \times 10^6$	$1.207 \pm 0.132$	1.153	1.159	1.155
$14.98 \pm 0.55$	$1.64 \times 10^6$	$1.22 \pm 0.25$	0.843	0.923	0.821
$18.99 \pm 0.65$	$8.49 \times 10^6$	$0.529 \pm 0.085$	0.214	0.499	0.225

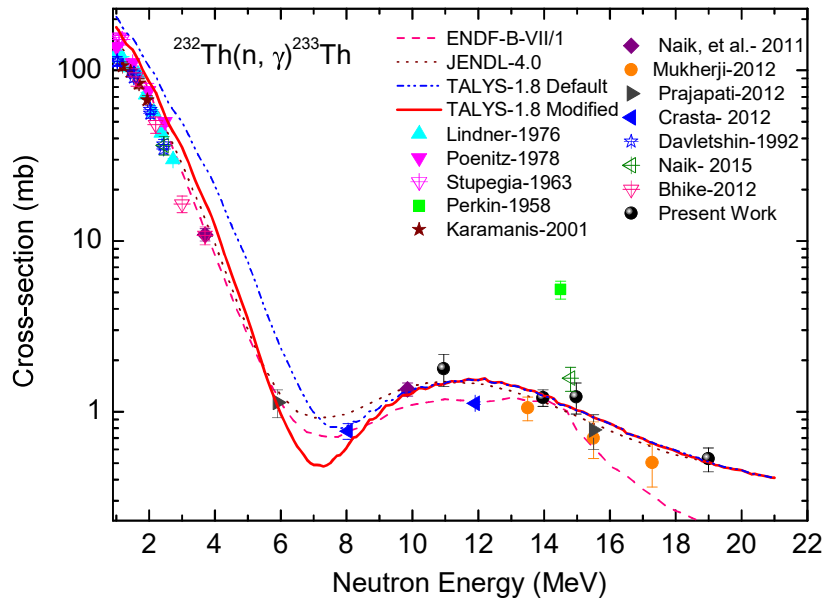


**Figure 5.9:** A comparison of the present results with the literature data [58–69], TALYS-1.8 [26] theoretical data (default as well as with modified parameter set) and the evaluated data from ENDF/B-VII.1 [50] and JENDL-4.0 [51] libraries.

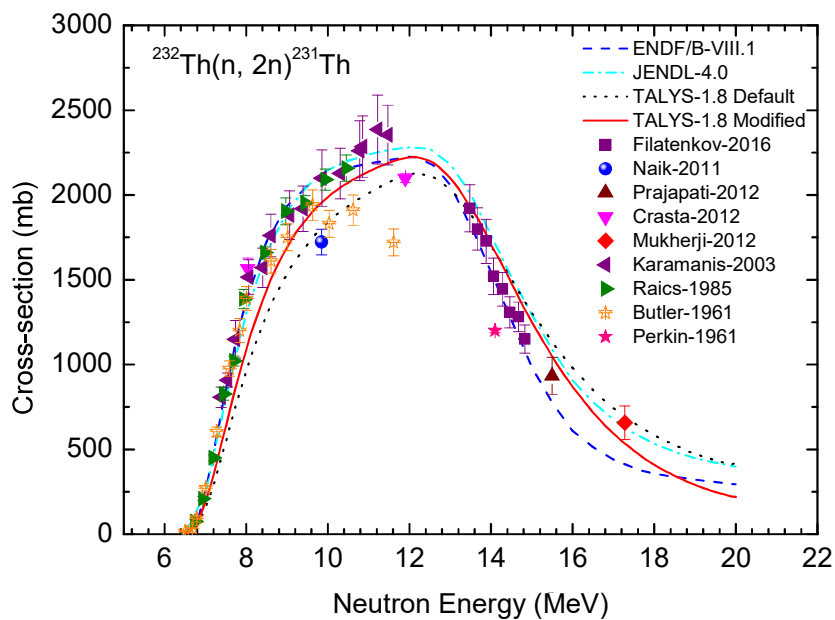


**Figure 5.10:** A comparison of the  $^{232}\text{Th}(n, 2n)^{231}\text{Th}$  data [58–61, 70–74] with the default and modified input parameter set of TALYS-1.8 [26], the evaluated data from ENDF/B-VII.1 [50] and JENDL-4.0 [51] libraries.

## 5.7 Excitation Function of the $^{232}\text{Th}(n, \gamma)^{233}\text{Th}$ Reaction

The excitation function of the  $^{232}\text{Th}(n, \gamma)^{233}\text{Th}$  reaction has measured at average neutron energies of  $10.95 \pm 0.59$ ,  $13.97 \pm 0.57$ ,  $14.98 \pm 0.55$ , and  $18.99 \pm 0.65$  MeV, respectively. The results are given in Table 5.15 and are plotted against the literature data [58–69], theoretical results from TALYS-1.8 [26] and the evaluated data from the ENDF/B-VII.1 [50], JENDL-4.0 [51] in Figure 5.9. It can be seen from the figure that the present results are in consensus with the literature data [58–69]. The  $^{232}\text{Th}(n, \gamma)$  reaction cross-sections starts to fall out as the incident energy increases beyond 1 MeV. A minima is achieved around 6 MeV as the  $^{232}\text{Th}(n, 2n)$  channel opens up. The (n, 2n) channel dominates at energies above 7 MeV. The cross-section data above 7 MeV are also found to be scarce with minor discrepancies. The use of different monitor reactions may lead to drastic change in reported data as the (n,  $\gamma$ ) cross-section is very sensitive at higher energies. The datum reported by Perkin et al., [62] shows a relatively higher cross-section value at 14.5 MeV using  $^{27}\text{Al}(n, \alpha)$  reaction as monitor. A correction for low energy neutrons was also applied<sup>16</sup>, however, the difference in the thresholds of monitor and sample reaction may lead to such higher value. The literature data [58–61, 63–69] except Perkin et. al., [62] were found to be in accordance with the theoretical reproductions of TALYS. The data from evaluated data libraries also found to be in agreement with the literature data [58–69]. Since, the  $^{232}\text{Th}(n, 2n)^{231}\text{Th}$  channel dominates in the considered energy range, therefore, the (n, 2n) channel has also been discussed and literature data [58–61, 70–74] were fitted with a modified set of input parameters of TALYS-1.8 [26].

A comparison of literature data of the  $^{232}\text{Th}(n, 2n)^{231}\text{Th}$  reaction cross-sections is shown in Figure 5.10. The reaction has a threshold of 6.0 MeV, as can be seen from the figure. The literature is found to be in a good agreement with the theoretical and the evaluated data. There are a few minor discrepancies can be observed in the cross-section values reported by Butler et al., [74] and Perkin et al., [73] with a comparatively larger errors by Karamanis et al., [70]. However, the ENDF/B-VII.1 [50] and JENDL-4.0 [51] were found to fit the measured data satisfactorily.

<sup>16</sup>The tailing correction is described in section 5.5

### 5.7.1 Theoretical Calculation within the Framework of TALYS-1.9 code

It can be seen from the figures 5.9 and 5.10, that the TALYS default values were not able to reproduce the data satisfactorily as seen previously for  $^{232}\text{Th}(n, \gamma)$  reaction. Therefore, a modified set of input level density parameters<sup>17</sup> was also used to find a better agreement of TALYS results with the  $(n, \gamma)$  and  $(n, 2n)$  reaction cross-sections for the entire range of energies under consideration. The modified parameter set used for the fitting of the data is given in Table 5.16. As can be seen from the table that only  $\gamma_1$  parameter from the equation 4.1 was modified to find a better fit for the  $(n, \gamma)$  reaction data. However, the  $(n, 2n)$  data was fitted by using the single particle level density parameter  $g$ , which can be defined as,  $g = A/k_{ph}$ , where  $A$  is atomic mass and  $K_{ph}$  is a constant. The  $K_{ph}$  is kept as 10 together with the modified value of  $\alpha$  from equation 4.1 to fit the  $(n, 2n)$  data more accurately. The  $\gamma$ -ray strength function  $f_{x\ell}(E_\gamma)$  for multipolarity  $\ell$  of type E or M were also calculated alongside the modified parameters by using a standard Lorentzian equation [75],

$$f_{x\ell}(E_\gamma) = K_{X\ell} \frac{\sigma_{X\ell} E_\gamma \Gamma_{X\ell}^2}{(E_\gamma^2 - E_{X\ell}^2)^2 + E_\gamma^2 \Gamma_{X\ell}^2} \quad (5.12)$$

The calculated  $\gamma$ -ray strength parameters for both the fittings are given in Table 5.17 in which, for  $E_1$  transitions the systematic formulas compiled by Kopecky [76] were used, whereas for  $E_2$  transitions the Brink-Axel [75] options were used as default by TALYS.

**Table 5.16:** Default and adjusted parameters used in the TALYS-1.8 calculations

parameter	CTM Collective		CTM Effective	
	Default Value	Adjusted Value for $^{232}\text{Th}(n, \gamma)$	Default Value	Adjusted value for $^{232}\text{Th}(n, 2n)$
$\alpha$	0.02073	0.02073	0.06926	0.01556
$\beta$	0.22953	0.22953	0.28277	0.28277
$\gamma_1$	0.47362	0.79462	0.4309	0.4309

<sup>17</sup>The level density parameters are discussed in subsection 4.1.1

**Table 5.17:**  $\gamma$ -ray strength function parameters for Giant Dipole Resonance

Multipole transition	$\gamma$ -ray strength function parameters			
	$\sigma_0(X\ell)$	$E(X\ell)$	$\Gamma(X\ell)$	$K(X\ell)$
M1	1.078	6.663	4.000	8.67E-08
E1	687.477	13.375	3.314	8.67E-08
M2	0.001	6.663	4.000	5.20E-08
E2	0.569	10.238	3.314	5.20E-08

## 5.8 Excitation Function of the $^{100}\text{Mo}(n, 2n)$ Reaction

The excitation function of the  $^{100}\text{Mo}(n, 2n)^{99}\text{Mo}$  reaction has been measured at average neutron energies of  $10.95 \pm 0.45$ ,  $13.97 \pm 0.68$ ,  $16.99 \pm 0.53$ , and  $20.00 \pm 0.58$  MeV, respectively, relative to the  $^{27}\text{Al}(n, \alpha)^{24}\text{Na}$  monitor reaction cross-sections. The uncertainties in the measurement were calculated by using covariance analysis similar to the  $^{232}\text{Th}(n, \gamma)$  reaction. Detailed calculations of error analysis are provided in Appendix A. The results are tabulated in Table 5.18 and are plotted in comparison with the theoretical data from TALYS-1.9 [26], ALICE-2014 [77,78], literature data [79–87], and with the evaluated data libraries like; ENDF/B-VII.1 [50], JENDL-4.0 [51], JEFF-3.2 [52], and CNEDL-3.1 [53], in Figures 5.11 and 5.12. It is obvious from the figure 5.11 that, the present results are in a good agreement with the literature and evaluated data libraries. Most of the experimental data are concentrated around 14 MeV only, with minor uncertainties. The literature data consist of the measurements done with the neutrons generated by D-D, D-T reactions [79–86] and  $^7\text{Li}(p, n)$  reaction [87]. The present data were also measured using  $^7\text{Li}(p, n)$  generated quasi-monoenergetic neutrons. Results from TALYS-1.9 default were also found fairly good in order to reproduce the overall trend of the data. The evaluated data were also found to reproduce the literature data satisfactorily as can be seen in figure 5.12. The uncertainties in present data were measured within the range of 12 – 18%. In which, a major contribution comes from the errors present in monitor reaction cross-section on evaluated data library ENDF/B-VII.1 [50].

### 5.8.1 Theoretical Calculation within the Framework of TALYS-1.9 and ALICE-2017 codes

The level density models (ldmodels 1-6) [88–93]<sup>18</sup> in TALYS-1.9 [26] were tested with ALICE-2017 [77, 78] to fit the present results. A comparison is shown in Figure 5.11. It can be observed from the figure that the ldmodels 1, 2, 4 and 5 [40, 41, 43, 44] are able to fit and follow the trend of the data more accurately than ldmodels 3 and 6 [42, 45], which are found to under-predict the reaction data up to  $\approx 15$  MeV than an over-prediction of the data can be observed. However, the experimental data can be fitted more precisely by using a modified set of input level density parameters as shown in Figure 5.12. The parameters used to fit the data are given in Table 5.19. ALICE [77, 78] was used to test and compare the results of TALYS code. The use of ALICE together with TALYS provides a test for the code as TALYS has been used commonly by different authors to predict light-ion induced reaction cross-section data, on the other hand, ALICE has been used extensively for heavy-ion induced reactions. ALICE successfully produced the trend and shape of the excitation function, however, the data values were marginally over-predicted within the energy range of 11-17 MeV. The over-prediction of the data may attribute to the over estimation of the compound nucleus process rather than pre-equilibrium. To check this with TALYS, the PE calculations were simply switched on and off within the input description of the code. The results of these calculations are plotted in Figure 5.13. It is evident from the figure that, there is a significant contribution from the PE process in the formation of the  $^{99}\text{Mo}$  isotope for the incident energies above 10 MeV. In comparison with ALICE, TALYS model code was found more suitable in order to reproduce the  $^{100}\text{Mo}(n, 2n)$  reaction data.

**Table 5.18:**  $^{100}\text{Mo}(n, 2n)^{99}\text{Mo}$  reaction cross-sections [22] compare with ENDF-B/VII.1, JENDL-4.0 and TALYS-1.9 data

$E_N$ (MeV)	Flux ( $n \text{ cm}^{-2}\text{s}^{-1}$ )	Cross-Section (mb)			
		Corrected	ENDF	JENDL	TALYS
$10.95 \pm 0.45$	$7.27 \times 10^5$	$1243.89 \pm 156.73$	1120.28	1092.62	1289.20
$13.97 \pm 0.68$	$1.48 \times 10^6$	$1422.53 \pm 190.61$	1478.30	1375.23	1533.38
$16.99 \pm 0.53$	$2.68 \times 10^6$	$1216.82 \pm 159.40$	1393.71	1326.21	1286.85
$20.00 \pm 0.58$	$3.09 \times 10^6$	$774.96 \pm 98.41$	612.44	925.11	671.88

<sup>18</sup>Details regarding the ldmodels in TALYS are given in subsection 4.1.1

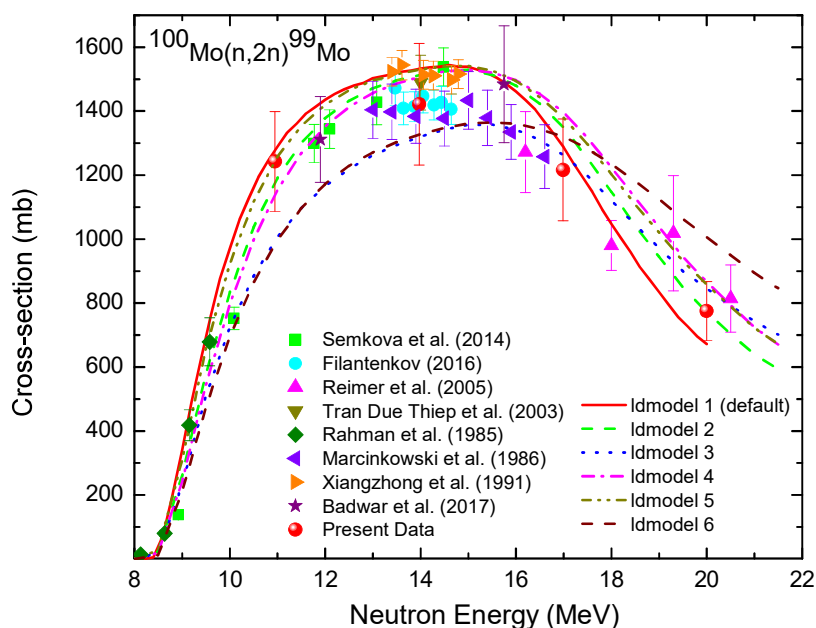


**Figure 5.11:** A comparison of the present results, literature data [79–87], and the theoretical results from different level density models (ldmodel 1-6) [40–45] of TALYS-1.9 [26] for  $^{100}\text{Mo}(n, 2n)^{99}\text{Mo}$  reaction.

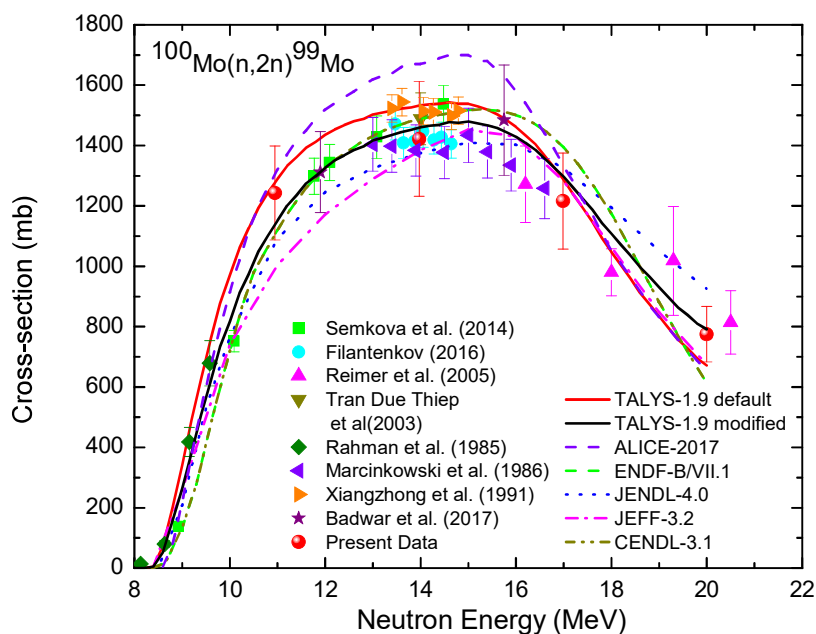


**Figure 5.12:** A comparison of the present results, literature data [79–87], evaluated data from ENDF/B-VII.1 [50], JENDL-4.0 [51], JEFF-3.2 [52], CENDL-3.1 [53] data libraries and the theoretical results from default and modified input level density parameters in TALYS-1.9 [26] for  $^{100}\text{Mo}(n, 2n)^{99}\text{Mo}$  reaction.

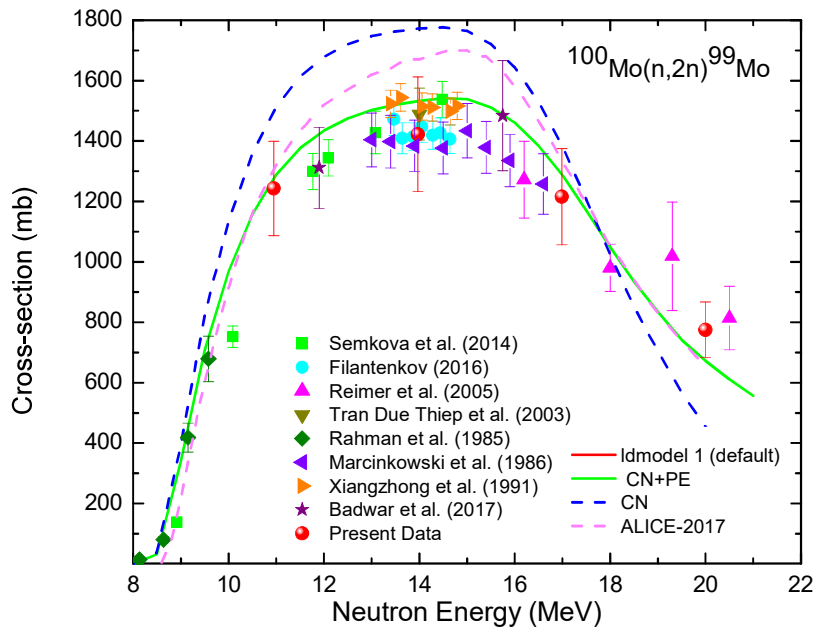


**Figure 5.13:** A comparison of the literature data [79–87] with PE calculations of TALYS-1.9 [26] and ALICE-2014 [77,78] (default) values.

**Table 5.19:** Default and adjusted parameters used in the TALYS-1.9 calculations

Parameter	CTM default	CTM adjusted
$\alpha$	0.06926	0.03974
$\beta$	0.28269	0.28269
$\gamma_1$	0.4331	0.04331

### 5.8.2 Calculation of $^{100}\text{Mo}(n, 2n)$ reaction cross-sections using systematic formulas around 14.5 MeV

In addition to the comparison of measured data with nuclear code, the experimentally measured (n, p), (n, 2n) and (n,  $\alpha$ ) reaction cross-section data of Mo isotopes available on EXFOR [57] data library were also compared with systematic formulas developed by different authors [28–38]. The systematic formulas for (n, p), (n, 2n) and (n,  $\alpha$ ) are listed in Tables 5.20, and 5.21, respectively. The calculated cross-section using given systematics for the

different isotopes produced via the  $(n, p)$ ,  $(n, 2n)$ , and  $(n, \alpha)$  reaction channels of Mo isotopes are listed in Table 5.22. The calculated cross-sections are compared with EXFOR data for respected isotope at 14.5 MeV. The table 5.22 shows that the calculated cross-sections are in agreement with each other and were found to be successful in reproducing experimental data, except for the results calculated using Forrest [32] and Bychkov [33] systematics. The results from Kasugai [30] and Luo [34] were measured as the closest to experimental data from EXFOR [57]. Among, the possible  $(n, 2n)$  reactions for Mo isotopes;  $^{94}\text{Mo}(n, 2n)^{93}\text{Mo}$  and  $^{100}\text{Mo}(n, 2n)^{99}\text{Mo}$ ; there is no datum available for the prior, however, the present measured datum for  $^{99}\text{Mo}$  isotope around 14 MeV is successfully reproduced by the systematic formulas. Furthermore, the literature data for the  $(n, \alpha)$  reaction cross-sections were also reproduced satisfactorily up to an acceptable degrees by using the systematics given in Table 5.21.

## 5.9 Excitation Function of the $^{58}\text{Ni}(n, x)$ Reaction

The excitation functions of the  $^{58}\text{Ni}(n, p)^{58}\text{Co}$  and  $^{58}\text{Ni}(n, 2n)^{57}\text{Ni}$  reactions were measured at average neutron energies within the range of 3-19 MeV relative to  $^{197}\text{Au}(n, \gamma)$ ,  $^{115}\text{In}(n, n')$  and  $^{27}\text{Al}(n, \alpha)$  monitor reactions as shown in Table 5.23. The uncertainties in the corrected cross-sections were calculated with covariance technique and were found to be in the range of 11 – 16%. The tailing corrected cross-sections with uncertainties are listed in Table 5.23 for both the reactions, however, the detailed calculations for generating covariance matrices for efficiency of the detector used and cross-sections are provided in Appendix A. The present results were compared with the literature data [11, 94–130], theoretical model predictions from TALYS-1.9 [26] & EMPIRE-3.2.3-Malta [27] codes using available input level density and PE models, ENDF/B-VII.1 [50], JENDL-4.0 [51], JEFF-3.2 [52], and CENDL-3.1 [53] evaluated data libraries. The results are plotted in the Figures 5.14-5.17. The excitation function of the  $^{58}\text{Ni}(n, p)^{58}\text{Co}$  reaction is shown in Figure 5.14. It can be observed from the figure that the present results are in agreement with the literature data [11, 94–122]. Among the five data points, the first two at neutron energies  $2.97 \pm 0.19$  and  $3.37 \pm 0.23$  MeV were measured relative to  $^{197}\text{Au}(n, \gamma)^{198}\text{Au}$  monitor reaction, whereas, the rest three at  $5.99 \pm 0.48$ ,  $13.97 \pm 0.68$ , and  $16.99 \pm 0.53$  MeV, respectively, were measured relative to  $^{115}\text{In}(n, n')^{115m}\text{In}$  reaction cross-sections. The present data agree well with the findings of previous measurements. The errors in the monitor cross-sections contribute to the larger uncertainties in the measured data above 5 MeV as compared to literature data. The errors in the reported cross-sections in literature were calculated by following

Table 5.20: Systematic formulas proposed by different authors for (n, p) and (n,2n) reactions

Author	Formula for $\sigma_{n,p}$	Mass region	n	Refs.
Levkovski	$\sigma_{n,p} = 50.21(A^{1/3} + 1)^2 \exp\left(-\frac{33.80(N-Z)}{A}\right)$	$40 \leq A \leq 209$	94	[28]
Ait-Tahar	$\sigma_{n,p} = 90.68(A^{1/3} + 1)^2 \exp\left(-\frac{34.48(N-Z+1)}{A}\right)$	$40 \leq A \leq 187$	86	[29]
Kasugai	$\sigma_{n,p} = 1264(N-Z+1) \exp\left(-\frac{46.63(N-Z+1)}{A}\right)$	$28 \leq A \leq 187$	89	[30]
Doczi	$\sigma_{n,p} = 18.12(A^{1/3} + 1)^2 \exp\left(-19.61 \frac{(N-Z)}{A} + \frac{(N-Z)^2}{A^2}\right)$	$28 \leq A \leq 209$	100	[31]
Forrest	$\sigma_{n,p} = 900(A^{1/3} + 1)^2 \exp\left(-49.27 \frac{(N-Z)}{A} + 197.1 \frac{(N-Z)^2}{A^2} - 0.45A^{1/2}\right)$	$40 \leq A \leq 187$	186	[32]
Bychkov	$\sigma_{n,p} = 7.06\pi r_0^2(A^{1/3} + 1)^2 \exp\sqrt{\frac{a}{E_n}} \left(\frac{0.58(Z-1)}{A^{1/3}} - \frac{50(N-Z+1)}{A} - 3.26\right)$	$28 \leq A \leq 209$	100	[33]
J. Luo	$\sigma_{n,p} = 62.98(A^{1/3} + 1)^2 \exp\left(-34.45 \frac{(N-Z)}{A}\right)$	$46 \leq A \leq 196$	36	[34]
Habbani	$\sigma_{n,p} = 60.34(A^{1/3} + 1)^2 \exp\left(-34.44 \frac{(N-Z+1)}{A}\right)$	$28 \leq A \leq 208(\text{even-A})$	23	[35]
	$\sigma_{n,p} = 20.91(A^{1/3} + 1)^2 \exp\left(-29.53 \frac{(N-Z)}{A}\right)$	$29 \leq A \leq 209(\text{odd-A})$	13	
Author	Formula for $\sigma_{n,2n}$	Mass region	n	Refs.
chatterjee	$\sigma_{n,2n} = 31.39(A^{1/3} + 1)^2 \exp\left(\frac{1.706(N-Z)}{A}\right)$	$45 \leq A \leq 238$	49	[36]
Lu and Fink	$\sigma_{n,2n} = 45.76(A^{1/3} + 1)^2 \left[1 - 7.372 \exp\left(-\frac{32.21(N-Z+1)}{A}\right)\right]$	$28 \leq Z \leq 82$	45	[37]
J. Luo	$\sigma_{n,2n} = 0.0226(A^{1/3} + 1)^2 \exp\left(\frac{133.86(N-Z)}{A} - \frac{779.47(N-Z)^2}{A^2} + \frac{1500.51(N-Z)^3}{A^3}\right)$	$23 \leq A \leq 209$	50	[34]
Bychkov	$\sigma_{n,2n} = 8.7(A + 100) \left[1 - 0.88 \exp\left(-\frac{7.95(N-Z)}{A}\right)\right]$	$45 \leq A \leq 238$	49	[33]
Habbani	$\sigma_{n,2n} = 23.53(A^{1/3} + 1)^2 \exp\left(3.50 \frac{(N-Z)}{A}\right)$	$45 \leq A \leq 209(\text{odd-A})$	10	[35]
	$\sigma_{n,2n} = 20.82(A^{1/3} + 1)^2 \exp\left(3.76 \frac{(N-Z+1)}{A}\right)$	$48 \leq A \leq 238(\text{even-A})$	39	

Table 5.21: Systematic formulas proposed by different authors for  $(n,\alpha)$  reaction

Author	Formula for $\sigma_{n,\alpha}$	Mass region	n	Refs.
Levkovski	$\sigma_{n,\alpha} = 16.55(A^{1/3} + 1)^2 \exp\left(-\frac{31.26(N-Z)}{A}\right)$	$31 \leq A \leq 202$	12	[28]
Ait-Tahar	$\sigma_{n,\alpha} = 31.66(A^{1/3} + 1)^2 \exp\left(-\frac{32.75(N-Z+1)}{A}\right)$	$40 \leq A \leq 188$	12	[29]
Kasugai	$\sigma_{n,\alpha} = 277.86 \exp\left(-\frac{24.66(N-Z)}{A}\right)$	$19 \leq A \leq 187$	12	[30]
Konobeyev	$\sigma_{n,\alpha} = 53.066(A^{1/3} + 1)^2 \exp\left(-209.11S^2 + 8.4723P - 0.19253Z/A^{1/3} - 0.96249\right)$ , $Z \leq 50$ $\sigma_{n,\alpha} = 53.066(A^{1/3} + 1)^2(-1.6462P + 0.39951)^3$ , $Z > 50$ $S = (N - Z + 1)/A$ , $P = (N - Z + 09.5)/A$	$40 \leq A \leq 209$ $40 \leq A \leq 209$	7 6	[38]
Forrest	$\sigma_{n,\alpha} = 24.71(A^{1/3} + 1)^2 \exp\left(-19.77\frac{(N-Z)}{A} + 13.82\frac{(N-Z)^2}{A^2} - 0.0248A\right)$	$20 \leq Z \leq 50$	7	[32]
J. Luo	$\sigma_{n,\alpha} = 20.91(A^{1/3} + 1)^2 \exp\left(-34.69\frac{(N-Z)}{A}\right)$	$50 \leq A \leq 206$	13	[34]
Habbani	$\sigma_{n,\alpha} = 3.6(A^{1/3} + 1)^2 \exp\left(-25\frac{(N-Z-3)}{A}\right)$	$26 \leq A \leq 238(\text{even-A})$	7	[35]

**Table 5.22:** Calculated  $(n, p)$ ,  $(n, 2n)$  and  $(n, \alpha)$  cross-sections using the systematic formulas given in Tables 5.20 and 5.21.

		$\sigma_{n,p}$ (mb) around 14.5 MeV									
A		Levkovski	Ait-Tahar	Kasugai	Doczi	Forrest	Bychkov	J. Luo	Habbani	EXFOR data	
	92	80.79	94.54	118.82	86.33	22.35	5.41	95.76	63.15	$72.0 \pm 3.0$	
	94	42.39	49.35	59.34	55.44	17.38	2.12	49.62	32.99	$54.3 \pm 5.4$	
	95	31.02	36.02	41.97	44.51	16.22	1.34	36.09	21.18	$41.0 \pm 5.5$	
	96	22.86	26.47	29.74	35.78	15.68	0.86	26.43	17.71	$25.6 \pm 0.8$	
	97	16.94	19.58	21.14	28.80	15.66	0.56	19.48	12.51	$16.67 \pm 1.20$	
	98	12.64	14.57	15.07	23.21	16.13	0.36	14.45	9.76	$5.3 \pm 0.5$	
	100	7.16	8.22	7.75	15.15	18.64	0.16	8.09	5.50	$6.2 \pm 1.4$	
A		$\sigma_{n,2n}$ (mb) around 14.5 MeV									
		chatterjee	Lu and Fink	J. Luo	Bychkov	Habbani	EXFOR data	Present data			
	94	1157.98	1070.62	955.40	1050.27	994.63	-	-			
	100	1312.62	1394.38	1451.00	1310.85	1255.70	$1503 \pm 45$	$1422.30 \pm 190.61$			
A		$\sigma_{n,\alpha}$ (mb) around 14.5 MeV									
		Levkovski	Ait-Tahar	Kasugai	Konobeyev	Forrest	J. Luo	Habbani	EXFOR data		
	92	33.21	39.09	26.69	30.39	15.27	31.14	28.13	$33.5 \pm 2.4$		
	98	5.99	6.63	6.73	2.88	5.39	4.64	6.85	$6.56 \pm 0.39$		
	100	3.54	3.85	4.41	1.09	3.97	2.59	4.44	$2.7 \pm 0.3$		

traditional method of taking the quadratic sum of systematic and statistical errors, which do not include the uncertainties present in monitor data. The present case shows the importance of detailed error analysis for the neutron data. The measured cross-sections largely depend on monitor data, which can be easily calculated by covariance method. It can also be observed from the figure 5.14 that, there exist a few minor discrepancies among the reported data [94, 102, 103, 107, 110, 116, 119]. However, most of the data follow the trend of the cross-sections very well. Evaluated data libraries; ENDF/B-VII.1 [50], JENDL-4.0 [51], JEFF-3.2 [52], and CENDL-3.1 [53] were also found successful in order to reproduce the literature data as can be seen from Figure 5.15.

**Table 5.23:** The Measured cross sections for the  $^{58}\text{Ni}(n, p)^{58}\text{Co}$  and  $^{58}\text{Ni}(n, 2n)^{57}\text{Ni}$  reactions [23]

Neutron Energy (MeV)	$^{58}\text{Ni}(n, p)^{58}\text{Co}$		$^{58}\text{Ni}(n, 2n)^{57}\text{Ni}$	
	Flux ( $ncm^{-2}s^{-1}$ )	Cross-section (mb)	Flux ( $ncm^{-2}s^{-1}$ )	Cross-section (mb)
$2.97 \pm 0.19$	$3.5 \times 10^6$	$198.07 \pm 23.37$	—	—
$3.37 \pm 0.23$	$3.8 \times 10^6$	$252.21 \pm 33.79$	—	—
$5.99 \pm 0.48$	$2.4 \times 10^6$	$547.32 \pm 76.07$	—	—
$13.97 \pm 0.68$	$3.2 \times 10^6$	$421.29 \pm 58.98$	$1.48 \times 10^6$	$31.28 \pm 4.16$
$16.99 \pm 0.53$	$6.05 \times 10^6$	$178.47 \pm 29.8$	$2.68 \times 10^6$	$65.67 \pm 9.59$

The  $^{58}\text{Ni}(n, 2n)^{57}\text{Ni}$  reaction cross-sections were measured at average neutron energies of  $13.97 \pm 0.68$ , and  $16.99 \pm 0.53$  MeV, relative to the  $^{27}\text{Al}(n, \alpha)^{24}\text{Na}$  monitor cross-sections. A comparison of the present results with the literature data is shown in Figure 5.16. Most of the literature data [11, 112–130] from the figure can be found to be concentrated around 14 MeV. The data [11, 114, 116, 119, 123, 124, 130] above 15 MeV contain minor discrepancies. The trend of the data above 15 MeV shows a general disagreement among the data from different authors [11, 116, 119, 123, 124, 130], which may attribute to the monitor reaction cross-sections. The present data were found in agreement with the literature data, except Refs. [114, 119, 123, 124, 130]. An uncertainty of  $\approx 2.5\%$  [50] from  $^{27}\text{Al}(n, \alpha)$  reaction attribute to the total uncertainty in the measured data. The evaluated data also found to be in accordance with the present and the literature data.

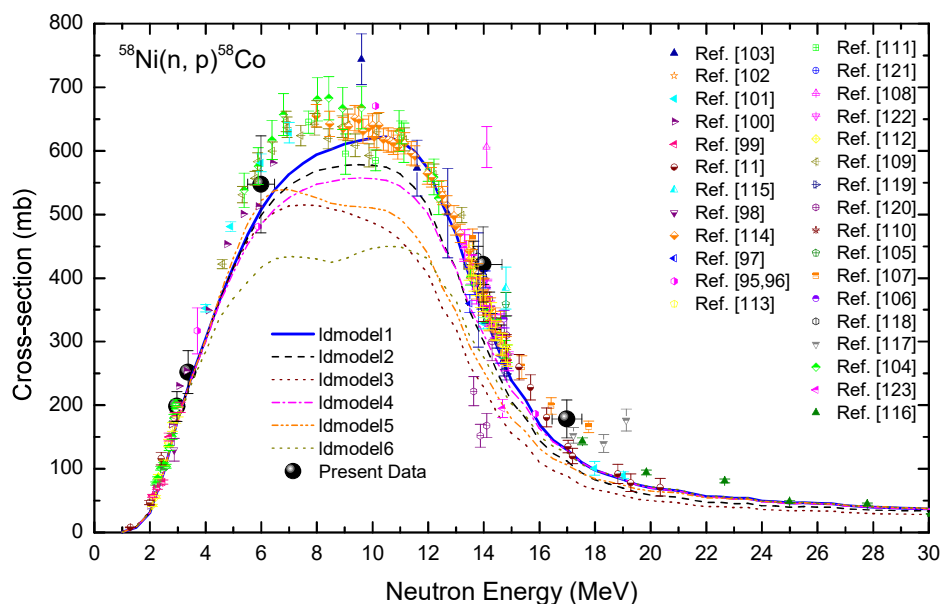


**Figure 5.14:** A comparison of present data with the literature data [11, 94–122] and the theoretical reaction cross-section calculations using the TALYS-1.9 [26] code.

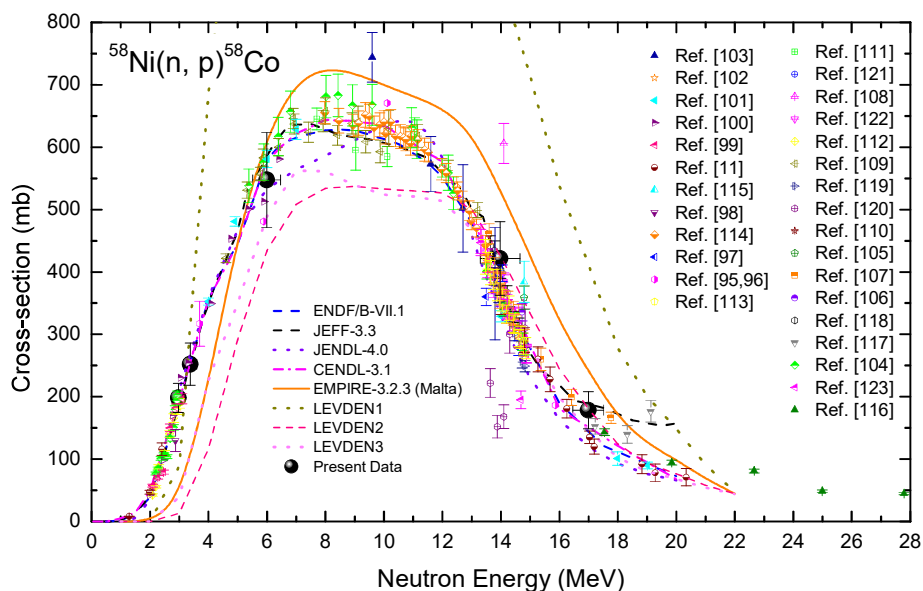


**Figure 5.15:** A comparison of present data with the literature data [11, 94–122], the evaluated data [50–53], and the theoretical reaction cross-section calculations using the EMPIRE-3.2.2-Malta [27] code.

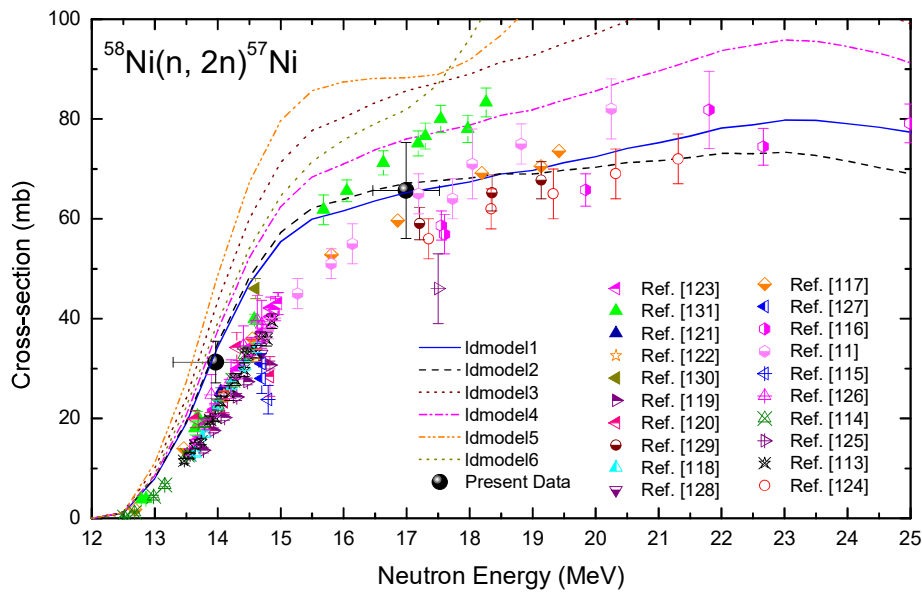


**Figure 5.16:** A comparison of present data with the literature data [11,112–130] and the theoretical reaction cross-section calculations using the TALYS-1.9 [26] code.

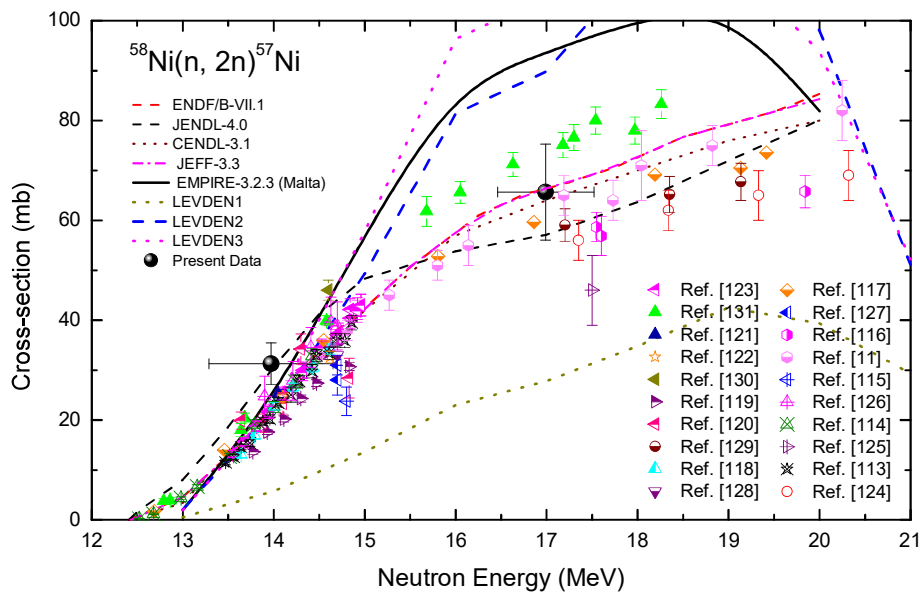


**Figure 5.17:** A comparison of present data with the literature data [11,112–130], the evaluated data [50–53], and the theoretical reaction cross-section calculations using the EMPIRE-3.2.2-Malta [27] codes.

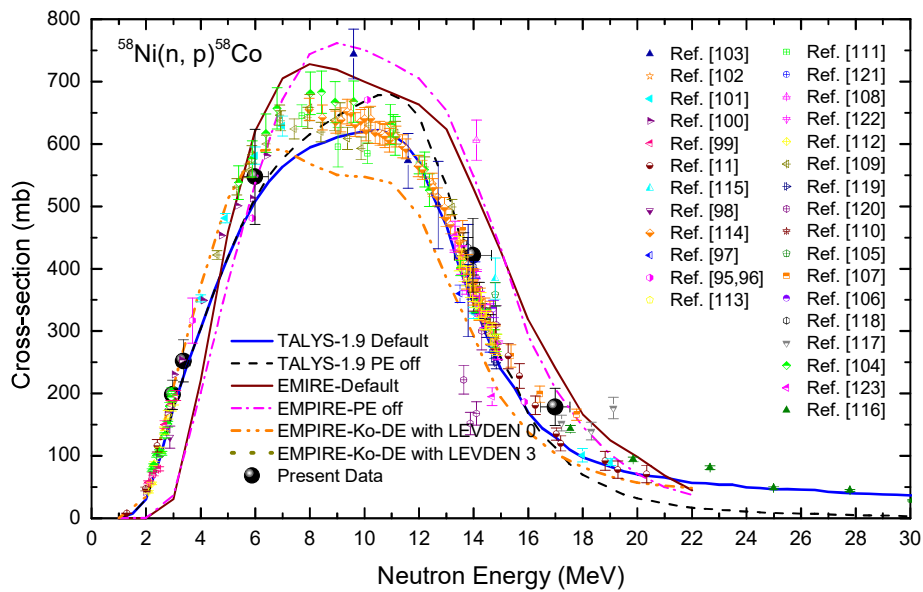


**Figure 5.18:** A comparison of present data with the literature data [11, 94–122], and the theoretical reaction cross-section calculations (default and by switching off the PE contribution) using the TALYS-1.9 [26] and EMPIRE-3.2.2-Malta [27] codes.

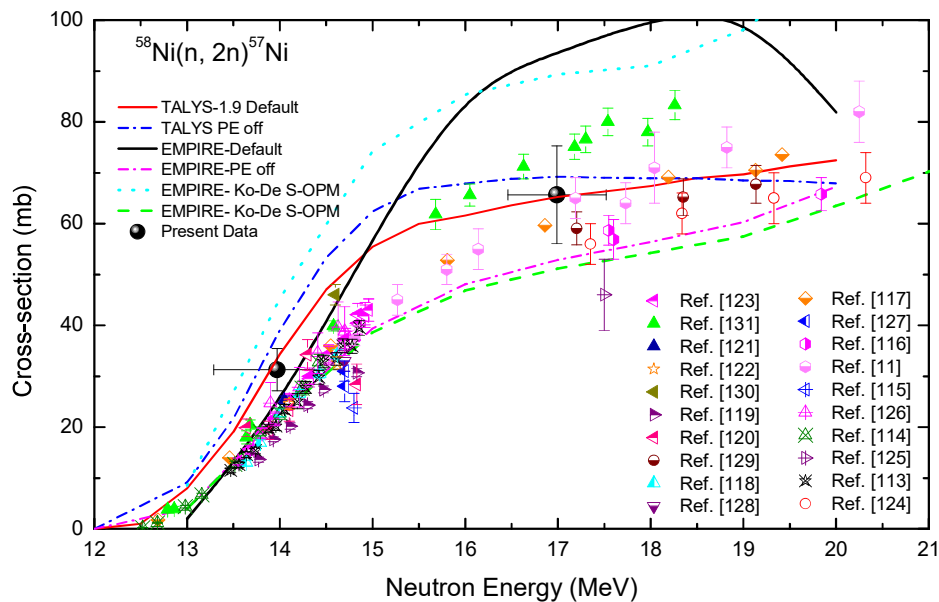


**Figure 5.19:** A comparison of present data with the literature data [11, 112–130], and the theoretical reaction cross-section calculations (default and by switching off the PE contribution) using the TALYS-1.9 [26] and EMPIRE-3.2.2-Malta [27] code.

**Table 5.24:** A comparison of the calculated  $[\sigma_{(n,p)}]$  results from different systematics with the data from EXFOR library at  $\approx 14.5$  MeV neutron energy.

Cross-Section $\sigma_{(n,p)}$ (mb)							
A	Levkovski	Ali-Tahar	Doczi	Habbani	Forrest	Measured Data at	
	[28]	[29]	[31]	[35]	[32]	14.5 MeV	14.6 MeV
112	45.49	56.172	59.951	29.934	48.512	No Data	$33.0 \pm 6.0$
114	27.053	33.214	41.492	22.218	49.512	No Data	$23.0 \pm 15.0$ $105.0 \pm 30.0$
115	21.006	25.724	34.566	15.269	50.512	No Data	$36.0 \pm 2.8$
116	16.383	20.012	28.824	13.395	51.512	$5.4 \pm 1.5$	$8.1 \pm 1.7$
117	12.832	15.636	24.06	9.938	52.512	$16.0 \pm 2.6$	$1.2 \pm 0.4$
118	10.093	12.268	20.104	8.216	9.601	No Data	$16.0 \pm 6.0$
119	7.971	9.666	16.816	6.564	6.958	$101.1 \pm 2.5$	No Data
120	6.32	7.646	14.081	5.124	5.048	$4.6 \pm 1.2$	$2.7 \pm 0.5$
122	4.02	4.841	9.906	3.245	2.664	No Data	$0.18 \pm 0.06$
124	2.594	3.11	7.000	2.087	1.413	No Data	No Data

**Table 5.25:** A comparison of the calculated  $[\sigma_{(n,2n)}]$  results from different systematics with the data from EXFOR library at  $\approx 14.5$  MeV neutron energy.

Cross-Section $\sigma_{(n,2n)}$ (mb)					
A	Chatterjee	Lu and Fink	Bychkov	Habbani	Measured Data at 14.5 MeV
	[36]	[37]	[33]	[35]	
112	1.2766	1.1878	1.1519	1.1598	No Data
114	1.3241	1.3444	1.2446	1.1681	No Data
115	1.3479	1.3993	1.2869	1.2768	No Data
116	1.3718	1.4434	1.3268	1.2477	No Data
117	1.3958	1.4794	1.3645	1.3579	No Data
118	1.4198	1.5091	1.4003	1.3299	$0.794 \pm 0.109$
119	1.4439	1.534	1.4341	1.4413	No Data
120	1.468	1.5551	1.4663	1.4149	No Data
122	1.5165	1.5893	1.5261	1.5024	No Data
124	1.5652	1.6163	1.5807	1.5925	No Data

### 5.9.1 Theoretical Calculation within the Framework of TALYS-1.9 and EMPIRE-3.2.3-Malta codes

The present results were compared with the theoretical data generated using TALYS-1.9 [26] and EMPIRE-3.2.3-Malta [27] codes. The level density models present in both the codes were tested to find a better agreement with the literature data for  $^{58}\text{Ni}(n, x)$  reactions. A comparison of theoretical results with the literature data is shown in Figures 5.14-5.17. It can be seen from the figures 5.14 and 5.15 that the TALYS is in better agreement with the literature data as compared to the EMPIRE reproductions. The level density models 1, 2 and 4 [40,41,43] were also found suitable to reproduce the reaction data, however, the rest of the ldmodels under-predicted the CN contribution to the (n, p) channel. On the other hand, the level density models from EMPIRE were only found to reproduce the trend of the cross-section data. Also, the distribution was found to be shifted towards the higher incident energies. A similar trend of both the codes can be seen from the figures 5.16 and 5.17 for  $^{58}\text{Ni}(n, 2n)$  data. The TALYS reproductions using ldmodel 1 and 2 [40,41] were found to be successful in order to fit the data accurately. On the other hand, none of the level density model from EMPIRE was able to fit the data accurately. The over-prediction showed by the EMPIRE results is due to the over estimation of the CN formation for both the reaction channels. To fit the data more precisely, the codes were tested with pure CN and CN+PE calculations. The results of PE calculations are plotted in Figures 5.18 and 5.19, for (n, p) and (n, 2n) channels, respectively. It is noted from the figure 5.18 that, both the codes over estimated the data after switching off the PE calculations. However, both the codes fit the literature data precisely by switching off the PE part of the calculations. The present exercise suggests that there may be minor contribution from the PE process in the formation of both  $^{58}\text{Co}$  and  $^{57}\text{Ni}$  isotopes. Also, TALYS has been found more suitable in order to fit the literature data.

## 5.10 Theoretical Study of the Reaction Cross-sections for Tin (Sn) isotopes

In addition to the experimental measurements of the reaction cross-sections of reactor isotopes, a theoretical calculation for tin isotopes was also carried out keeping the importance of those in mind. A rigorous literature survey for the neutron induced reactions of Sn isotopes shows that most of the data [133–144] are concentrated only around 14 MeV [57]. Sn being

a magic nucleus shows considerably less neutron capture cross-section, which makes the experimental study of the n-induced reactions, tedious. An attempt has been made to test the nuclear model codes, TALYS [26] and EMPIRE [27], in order to produce the available literature data precisely. This present a test for the nuclear model codes so that users can be confident to use the codes to predict the reaction cross-section data. In order to do so, the level density models available in both the codes were used to fit the literature data. The comparison of the literature data with TALYS [26] and EMPIRE [27] are plotted in Figures 5.20-5.25. The ENDF/B-VII.1 [50] evaluated data have been used as reference for each comparison. Furthermore, different systematics [28,29,31–33,35–37] given in Table 5.20 were also used to reproduce the (n, p) and (n, 2n) reaction literature data at 14.5 MeV incident neutron energy. The doubly-magic nature of the nuclei makes the case more interesting. The results calculated using systematics are given in Tables 5.24 and 5.25, respectively, for (n, p) and (n, 2n) reaction cross-sections. From Table 5.24, it can be observed that the systematic data are in a fair agreement with the experimentally measured cross-section data. It can be observed from both the tables that a very limited amount of data are available for the neutron induced reactions on Sn isotopes.

The theoretically calculated cross-sections using different level density models from both TALYS and EMPIRE are plotted in Figures 5.20-5.25, for  $^{116}\text{Sn}(n, p)^{116}\text{In}$ ,  $^{117}\text{Sn}(n, p)^{117}\text{In}$ ,  $^{117}\text{Sn}(n, p)^{117m}\text{In}$ ,  $^{118}\text{Sn}(n, 2n)^{117m}\text{Sn}$ ,  $^{120}\text{Sn}(n, 2n)^{119m}\text{Sn}$ , and  $^{124}\text{Sn}(n, 2n)^{123m}\text{Sn}$  reactions, respectively. In general, it can be observed from the figures that the data have only been measured around 14 MeV incident neutron energies. The mono-energetic sources have been used for the experimental studies. There are minor uncertainties present in the data for the  $^{117}\text{Sn}(n, p)^{117,117m}\text{In}$  and  $^{124}\text{Sn}(n, 2n)^{123m}\text{Sn}$  reactions, as can be seen from the figures 5.21, 5.22, and 5.25, respectively. On the other hand, only one experimental measurement is available for the  $^{120}\text{Sn}(n, 2n)^{119m}\text{Sn}$  reaction. It can be seen from the figure 5.20 that none of the level density model (LEV DEN 0-3) [40–42, 131, 132] from EMPIRE is found to fit the data satisfactorily, however, the level density model 4,5 (ldmodel-4,5) [43, 44] were found to be able to reproduce the data up to an acceptable degree. A general disagreement among the different measured data can be observed from the figure 5.21. All the level density models from both the codes were found to reproduce the trend of the data [134–141] and the ENDF/B-VII.1 [50] data, except the LEV DEN-1 and 2 [40, 41] from the EMPIRE [27] code. The comparison of  $^{117}\text{Sn}(n, p)^{117m}\text{In}$  reaction data [134–141] with theoretical results is plotted in figure 5.22. It can be observed that the only data from Hasan et al., [139] matches with the ENDF/B-VII.1 [50] results. The data from Ikeda et al., [134] produces a

trend of cross-sections within 13-15 MeV energies. Depending upon which, the TALYS level density models were found suitable for the fitting of the available data keeping the fact that TALYS values do not match with the ENDF data. The EMPIRE calculation results were found to follow the trend of ENDF data, except LEVDEN-2. Depending upon the trend of all the measured reaction data, TALYS results were found satisfactory to reproduce the measured data.

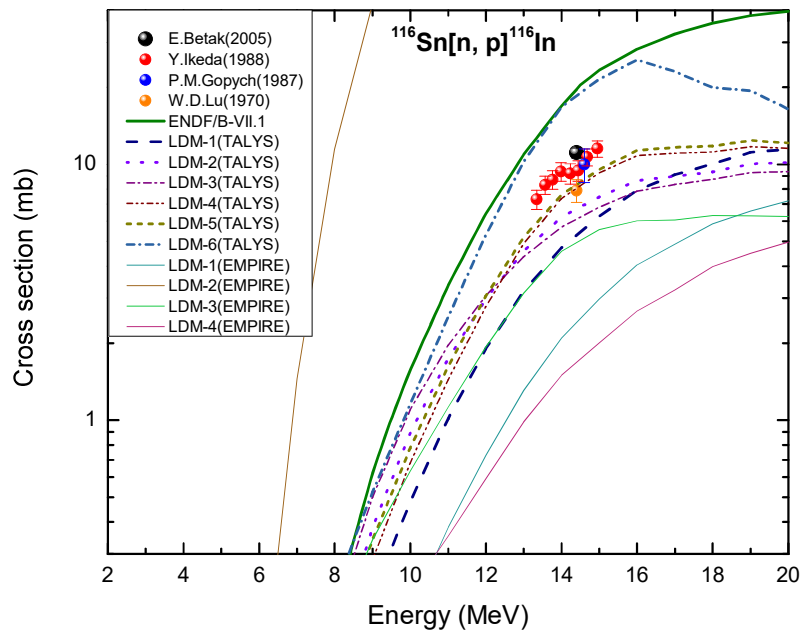


**Figure 5.20:** Experimental cross-sections for  $^{116}\text{Sn}(n, p)^{116}\text{In}$  reaction fitted with ENDF/B-VII.1 [50] and different level density parameters using TALYS-1.8 [26] and EMPIRE-3.2.2 [27].

The  $(n, 2n)$  reaction cross-sections for  $^{118,120,124}\text{Sn}$  isotopes are plotted in Figures 5.23, 5.24, and 5.25, respectively. The theoretical reproductions from TALYS [26] and EMPIRE [27] were found to follow the trend of experimental data. The evaluated data from ENDF/B-VII.1 [50] were found to be higher than the theoretical and measured data by an order of 2. However, the ldmmodel-5 from TALYS and LEVDEN-1,4 were found to be successful for the reproduction of the data. A comparison of the measured data for  $^{120}\text{Sn}(n, 2n)^{119m}\text{Sn}$  reaction taken from the EXFOR library, are plotted in figure 5.24. There is only one data point by Lulic et al., [140] available for the present reaction, which agrees well with the ENDF/B-VII.1 [50] evaluated data. The TALYS and EMPIRE values were found to produce the trend of the ENDF data. A concrete conclusion can not be made due to the scarcity

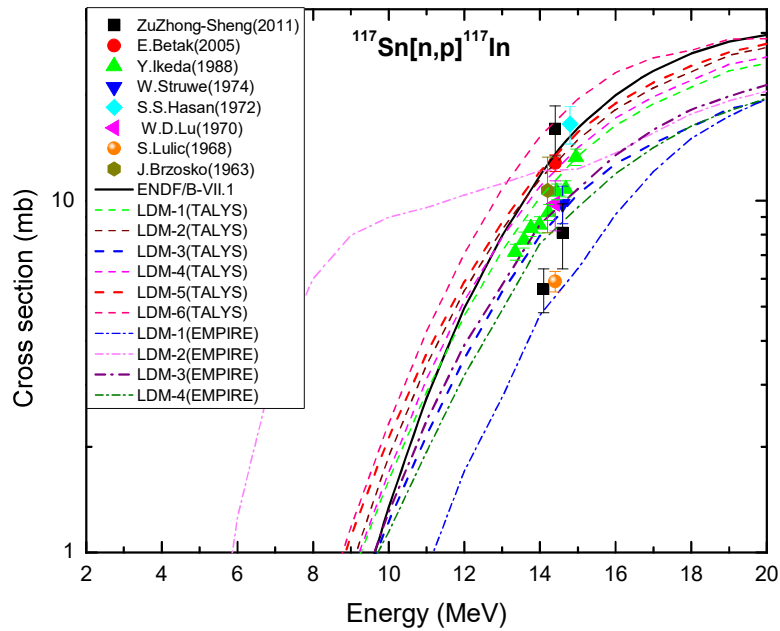


**Figure 5.21:** Experimental cross-sections for  $^{117}\text{Sn}(n, p)^{117}\text{In}$  reaction fitted with ENDF/B-VII.1 [50] and different level density parameters using TALYS-1.8 [26] and EMPIRE-3.2.2 [27].

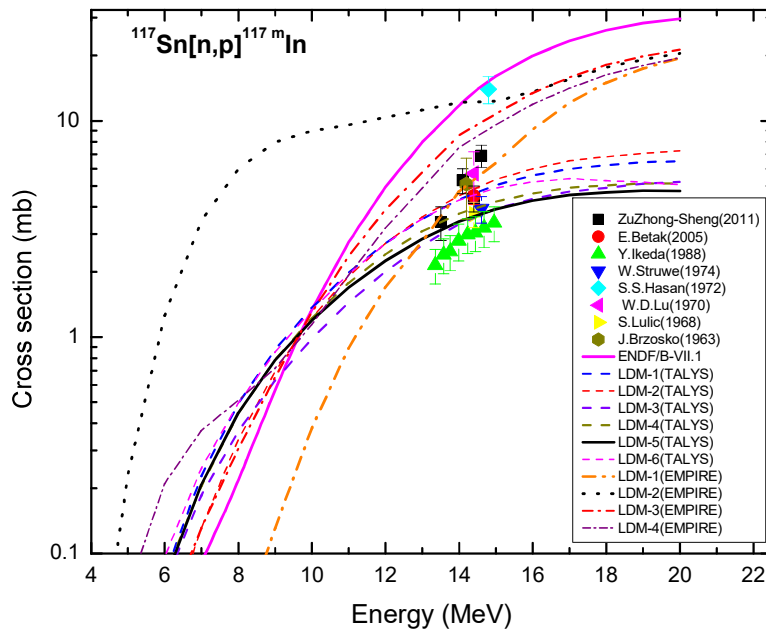


**Figure 5.22:** Experimental cross-sections for  $^{117}\text{Sn}(n, p)^{117m}\text{In}$  reaction fitted with ENDF/B-VII.1 [50] and different level density parameters using TALYS-1.8 [26] and EMPIRE-3.2.2 [27].

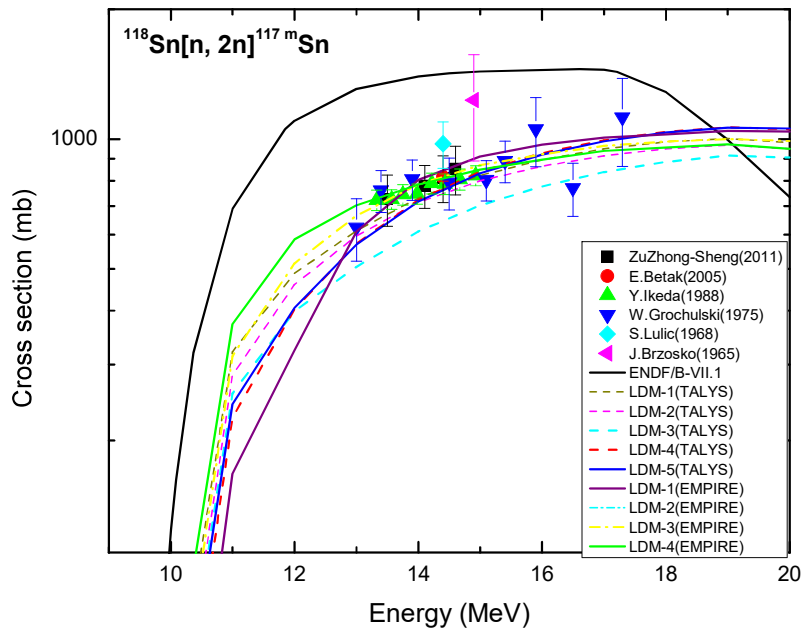


**Figure 5.23:** Experimental cross-sections for  $^{118}\text{Sn}(n, 2n)^{117m}\text{Sn}$  reaction fitted with ENDF/B-VII.1 [50] and different level density parameters using TALYS-1.8 [26] and EMPIRE-3.2.2 [27].

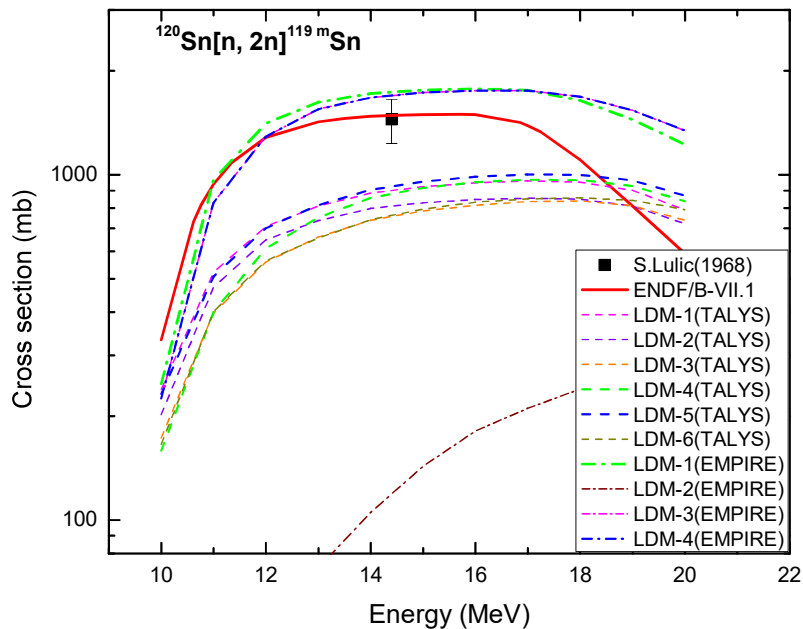


**Figure 5.24:** Experimental cross-sections for  $^{120}\text{Sn}(n, 2n)^{119m}\text{Sn}$  reaction fitted with ENDF/B-VII.1 [50] and different level density parameters using TALYS-1.8 [26] and EMPIRE-3.2.2 [27].

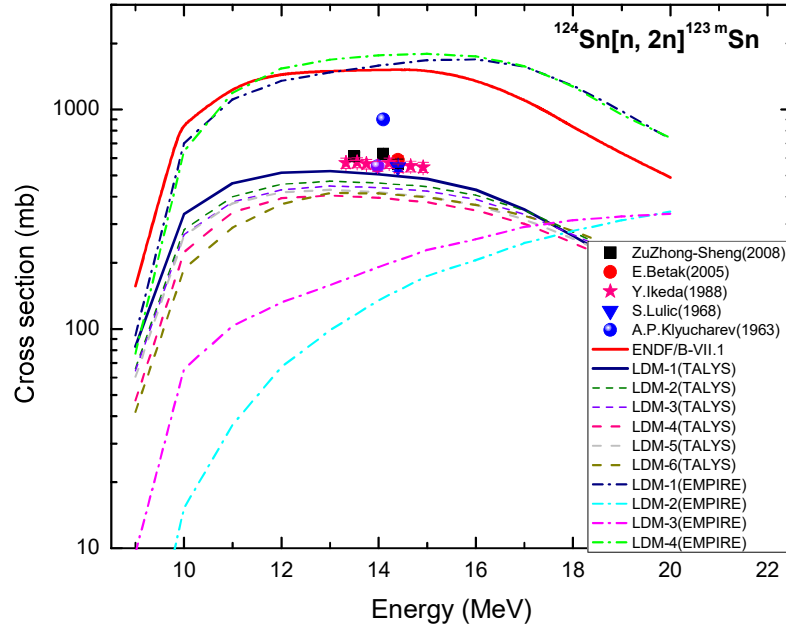


**Figure 5.25:** Experimental cross-sections for  $^{124}\text{Sn}(n, 2n)^{123m}\text{Sn}$  reaction fitted with ENDF/B-VII.1 [50] and different level density parameters using TALYS-1.8 [26] and EMPIRE-3.2.2 [27].

of the data for the present case. The experimental  $^{124}\text{Sn}(n, 2n)^{123m}\text{Sn}$  reaction cross-section data compared with the evaluated and theoretical data are plotted in Figure 5.25. It can be observed from the figure that the measured data are in accordance among each other and with ldmodel-1 from TALYS, except the data from Klyucharev et al., [144]. The results from EMPIRE were found either over-predicting or under-predicting the data. Based on the discussion provided above, the TALYS nuclear model code was found better for the prediction of the presented data.



# Bibliography

- [1] Extending the global reach of nuclear energy through Thorium, Published by S.K. Malhotra, Head, Public Awareness Division, D.A.E, Govt. of. India, September 2008, [http://dae.nic.in/writereaddata/.pdf\\_38](http://dae.nic.in/writereaddata/.pdf_38).
- [2] C. Rubbia, J.A. Rubio, S. Buono, F. Carminati, N. Fietier, J. Galvez, C. Geles, Y. Kadi, R. Klapisch, P. Mandrillon, J.P. Revol, Ch. Roche, Conceptual Design Of a Fast Neutron Operated High Power Energy Amplifier, CERN Report No. CERN/AT/95-44 (ET) (1995).
- [3] C.D. Bowman, et al., Nuclear Energy Generation and Waste Transmutation Using an Accelerator-Driven Intense Thermal Neutron Source, Los Alamos National Laboratory Report LA-UR-91-2601 (1991).
- [4] C.D. Bowman, Ann. Rev. Nucl. Part. Sci. **48**, (1998) 505.
- [5] F. Carminati, R. Klapisch, J.P. Revol, Ch. Roche, J.A. Rubio, C. Rubbia, An Energy Amplifier for Cleaner and Inexhaustible Nuclear Energy Production Driven by Particle Beam Accelerator, CERN Report No. CERN/AT/93-47 (ET) (1993).
- [6] E.D. Arthur, S.A. Schriber, A. Rodriguez (Editors), The International Conference on Accelerator-Driven Transmutation Technologies and Applications, Las Vegas, Nevada, USA, 1994, AIP Conf. Proc., Vol. **346** (1995).
- [7] Accelerator Driven Systems: Energy Generation and Transmutation of Nuclear Waste, Status report: IAEA TECDOC-985 (1997).
- [8] S. Ganesan, Pramana J. Phys. **68**, (2007) 257.
- [9] World Thorium Deposits and Resources, Integrated Nuclear Fuel Cycle Information Systems, IAEA <https://infcis.iaea.org/THDEPO/About.cshtml>
- [10] S. Parashari et al., *Phys. Rev. C* **98** (2018) 014625.

- [11] V. Semkova, V. Avrigeanu, T. Glodariu, A.J. Koning, A.J.M. Plompen, D.L. Smith, S. Sudar, *Nuclear Physics A* **730** (2004) 255.
- [12] C.L. Whitmarsh, Oak Ridge National Laboratory Report: ORNL-3281, UC-80-Reactor technology, TID-4500 (17th ed.).
- [13] U. Fischer, P. Batistoni, E. Cheng, R. A. Forrest, T. Nishitani, *Proc. International conference on nuclear data for science and technology* vol **769** (AIP Conf. ) (2005) 1478.
- [14] T. Ruth, 2009. *Nature* **457**, (2009) 536.
- [15] International Atomic Energy Agency, *Nuclear Technology Review, Annex VIII: Production and Supply of Molybdenum-99*, (2008). IAEA/NTR/2010, Vienna, 50.
- [16] *Medical Isotope Production Without Enriched Uranium, Alternative molybdenum- 99 production process*, (2009). <http://www.nap.edu/openbook.phn>.
- [17] K. Gagnon et al., *J. Nucl. Med. Biol.* **38**, (2011) 907.
- [18] S. Takacs, et al., *J. Radioanal. Nucl. Chem* **257** (2003) 195.
- [19] Lagunas-Solar, et al., *Am. Nucl. Soc.* **74**, (1996) 134.
- [20] D.L. Mollin, *Proc. R. Soc. Med.*, **55** (2) (1962) 141.
- [21] Y. Takahashi et al., *Japan. Nucl. Fusion* **51** (113015) (2011) 11.
- [22] S. Parashari et al., *Phys. Rev. C* **99** (2019) 044602.
- [23] S. Parashari et al., *Eur. Phys. Jour. A* **55** (2019) 51.
- [24] N. Otuka, B. Lalremruata, M.U. Khandaker, A.R. Usmand, L.R.M. Punte, *Radiat. Phys. Chem.*, **502** (2017) 140.
- [25] S. Parashari et al., *App. Rad. Iso.* **133** (2018) 31.
- [26] A. J. Koning, S. Hilaire, S. Goriely, *TALYS user manual, A nuclear reaction program, NRG-1755 ZG PETTEN*, The Netherlands (2015).
- [27] M. Herman, R. Capote, M. Sin, A. Trkov, B.V. Carlson, P. Oblozinsky, C.M. Mattoon, H. Wienkey, S. Hoblit, Young-Sik Cho, G.P.A. Nobre, V.A. Plujko, V. Zerkin, *EMPIRE-3.2 Malta modular system for nuclear reaction calculations and nuclear data evaluation, user manual, INDC(NDS)-0603, BNL-101378-2013* (2014).

- [28] V.N. Levkovski, Zh. Eksp. Teor. Fiz. **45** (1963) 305.
- [29] S. Ait-Tahar, Nucl. Phys. **13** (1987) 121.
- [30] Y. Kasugai, Y. Ikeda, H. Yamamoto, K. Kawade, in: JAERI-Conf. 95-008, (1995).
- [31] R. Doczi, V. Semkova, A.D. Majdeddin, Cs.M. Buczko, J. Csikai, Indc(HUN)-032,NDS, IAEA, (1997).
- [32] R.A. Forrest, D.A.J. Endacott, Activation Elements Relevant to Fusion Reactors, Harwell Laboratory Report, AERE R 13402 (1989).
- [33] V.M. Bychkov, V.N. Manokhin, A.B. Pashchenko, V.I. Plyashin, Indc(CCP)-146, NDS, IAEA, (1980).
- [34] J. Luo et al. Nucl. Instr. and Meth. in Phys. Res. B **266** (2008) 4862.
- [35] F.I. Habbani, Khalda T. Osman, Appl. Radiat. Isotopes **54** (2001) 83.
- [36] S. Chatterjee, A. Chatterjee, Nucl. Phys. A **125** (1969) 593.
- [37] Wen-deh Lu, R.W. Fink, Phys. Rev. C **4** (1971) 1173.
- [38] A.Yu. Konobeyev, V.P. Lunev, Yu.N. Shubin, Nucl. Instr. and Meth. B **108** (1996) 233.
- [39] Qtool: calculation of reaction Q-values and threshold, Los Alamos National Library, [http://cdfesinp.msu.ru/services/calc\\_thr/calc\\_thr.html](http://cdfesinp.msu.ru/services/calc_thr/calc_thr.html).
- [40] NuDat 2.7 $\beta$  2011, *National Nuclear Data Center, Brookhaven National Laboratory*, <http://www.nndc.bnl.gov/>.
- [41] H. Liskien, A. Paulsen, At. Data Nucl. Data Tables **15** (1975) 57.
- [42] J.W. Meadows, D.L. Smith, Neutrons from proton bombardment of natural Lithium, Argonne National Laboratory Report ANL-7983 (1972).
- [43] C.H. Poppe, J.D. Anderson, J.C. Davis, S.M. Grimes, C. Wong, Phys. Rev. C **14** (1976) 438 .
- [44] H. Naik, P.M. Prajapati, S.V. Surayanarayana, K.C. Jagadeesan, S.V. Thakare, D. Raj, V.K. Mulik, B.S. Sivashankar, B.K. Nayak, S.C. Sharma, S. Mukherjee, Sarbjit Singh, A. Goswami, S. Ganesan, V.K. Manchanda, Eur. Phys. J. A **47** (2011) 51.

- [45] S. Parashari, S. Mukherjee, A.P. Singh, Vibha Vansola, H. Naik, B.K. Nayak, Rajnikant Makwana, S.V. Suryanarayana, N.L. Singh, Mayur Mehta, Y.S. Sheela, M. Karkera, R.D. Chauhan, S. C. Sharma Phys. Rev. C **98** (2018) 014625.
- [46] R. Makwana, S. Mukherjee, P. Mishra, H. Naik, N.L. Singh, M. Mehta, K. Katovsky, S.V. Suryanarayana, V. Vansola, Y. Santhi Sheela, M. Karkera, R. Acharya, S. Khirwadkar Phys. Rev. C **96** (2017) 024608.
- [47] B.S. Shivashankar, H. Naik, N. Sreekumaran Nair, S. Ganesan, S. V. Suryanarayana, K. Manjunatha Prasad, Nucl. Sci. and Eng., **179**, (2015) 423. DOI: 10.13182/NSE14-19.
- [48] B.S. Shivashankar H. Naik, S.V. Suryanarayana, P.M. Prajapati, V.K. Mulik, K.C. Jagadeesan, S.V. Thakare, A. Goswami, S. Ganesan, Jour. of Radioanalytical and Nuclear Chemistry, **292**, (2012) 745. DOI: 10.1007/s10967-012-1646-9.
- [49] M. Bhike, A. Saxena, B.K. Nayak, S. Ganesan, B. Lalremruata, R. Palit, R. Tripathi, S. Sodaye, A.V.R. Reddy, S. Kailas, R.K. Choudhury, conf. Nucl. Data for Adv. Nucl. Systems, Mangalore, India, 2006, p.(TP15) (2006).
- [50] ENDF/B-VII.1, 2011, National Nuclear Data Center, Brookhaven National Laboratory, <http://www.nndc.bnl.gov/exfor/endlf00.jsp>
- [51] K. Shibata, O. Iwamoto, T. Nakagawa, N. Iwamoto, A. Ichihara, S. Kunieda, S. Chiba, K. Furutaka, N. Otuka, T. Ohasawa, T. Murata, H. Matsunobu, A. Zukeran, S. Kamada, J. Nucl. Sci. Technol. **48** (2011).
- [52] A.J. Koning, E. Bauge, C.J. Dean, E. Dupont, U. Fischer, R.A. Forrest, R. Jacqmin, H. Leeb, M.A. Kellet, R.W. Mills, C. Nordborg, M. Pescarini, Y. Rugama, P. Rullhusen, Status of the JEFF nuclear data library. J. Kor. Phys. Soc. **59** issue 2 (2011) 1057.
- [53] Z.G. Ge, Z.X. Zhao, H.H. Xia, Y.X. Zhuang, T.J. Liu, J.S. Zhang, H.C. Wu, Updated Version of Chinese Evaluated Nuclear Data Library (CENDL-3.1). J. Kor. Phys. Soc. **59** (2), (2011) 1052.
- [54] B. Soni et al., "Measurement of (n, xn) reaction cross-sections on  $^{113,115}\text{In}$  isotopes using quasi-monoenergetic neutrons within 10-20 MeV" Submitted in Eur. Phys. Jour. P (2019).
- [55] S. Mukherji, H. Naik, and S.V. Suryanarayana, Proc. DAE Symp. Nucl. Phys. **59**, (2014) 426 .

- [56] D.L.Smith, J.W. Meadows, P.A. Moldauer, and W.P. Poenitz, Nucl. Phys. A **388**, (1982) 37.
- [57] IAEA-EXFOR experimental nuclear reaction data base, <http://www.nds.iaea.org/exfor>.
- [58] H. Naik, P. M. Prajapati, S. V. Surayanarayana, K. C. Jagadeesan, S. V. Thakare, D. Raj, V. K. Mulik, B. S. Shivashankar, B. K. Nayak, S.C. Sharma, S. Mukherjee, Sarbjit Singh, A. Goswami, S. Ganesan, V. K. Manchanda, Eur. Phys. J. A **47**, (2011) 51 .
- [59] S. Mukherji, H. Naik, S.V. Suryanarayanan, S. Chachara, B. S. Shivashankar, V. Mulik, Rita Crasta, SudiptaSamanta, B. K. Nayak, A. Saxena, S.C. Sharma, P.V. Bhagwat, K.K. Rasheed, R.N. Jindal , S. Ganeshan, A. K. Mohantey, A. Goswami, P.D. Krishnani, Pramana **79**, (2012) 249.
- [60] P. M. Prajapati, H. Naik, S. V. Suryanarayana, S. Mukherjee, K. C. Jagadeesan, S. C. Sharma, S. V. Thakre, K. K. Rasheed, S. Ganesan, A. Goswami, Eur. Phys. J. A **48**, (2012) 35 .
- [61] R. Crasta, H. Naik, S. V. Suryanarayana, B. S. Shivashankar, V. K. Mulik, P. M. Prajapati, G. Sanjeev, S. C. Sharma, P. V. Bhagwat, A. K. Mohanty, S. Ganesan, A. Goswami, Ann. of Nucl. Energy **47**, (2012) 160 .
- [62] J. L. Perkin, L. P. O'Connor, R. F. Colemann, Proc. Phys. Soc. London **72**, (1958) 505 .
- [63] D. C. Stupegia, B. Smith, K. Hamm, J. Inorg. Nucl. Chem. **25**, (1963) 627 .
- [64] M. Lindner, R. J. Nagle, J. H. Landrum, Nucl. Sci. Eng. **59**, (1976) 381 .
- [65] H. Naik, S. V. Surayanarayana, S. Bishnoi, et al., J. Radioanal. Nucl. Chem. **303** (2015) 2497 .
- [66] M. Bhike, B. J. Roy, A. Saxena, R. K. Choudhury, S. Ganesan, J. Nuclear Science and Engineering, **170**, (2012) 44 .
- [67] W. P. Poenitz, D.L. Smith, Fast neutron radiative capture cross sections of  $^{232}\text{Th}$ , Rept., ANL-NDM-42,197803, Argonne National Laboratory Reports, No. 42 (1978).
- [68] A. N. Davletshin, E. V. Teplov, A. O. Tipunkov, V. A. Tolstikov, I. A. Korzh, V. D. Ovdienko, N. M. Pravdivyy, N. T. Sklyar, V. A. Mishchenko, J. YadernyeKonstanty, **41** (1992).

- [69] D. Karamanis, M. Petit, S. Andriamonje, G. Barreau, M. Bercion, A. Billebaud, B. Blank, S. Czajkowski, R. Del Moral, J. Giovinazzo, V. Lacoste, C. Marchand, L. Perrot, M. Pravikoff, J.C. Thomas, Nucl. Sci. Eng. **139**, (2001) 282.
- [70] D. Karamanis, S. Andriamonje, P.A. Assimakopoulos, G. Doukellis, D. A. Karadimos, A. Karydas, M. Kokkoris, S. Kossionides, N. G. Nicolis, C. Papachristodoulou, C. T. Papadopoulos, N. Patronis, P. Pavlopoulos, G. Perdikakis, R. Vlastou, and the n-TOF Collaboration, Nucl. Instrum. Methods in Physics Res. A **505**, (2003) 381.
- [71] A.A. Filatenkov, Rept: USSR report to the INDC., No. 0460 (2016).
- [72] P. Raics, S. Daroczy, J. Csikai, N. V. Kornilov, V. Ya. Baryba, O. A. Salnikov, Phys. Rev. C **32**, (1985) 87 .
- [73] J. L. Perkin, R.F. Coleman, Nucl. Energy A&B (Reactor Sci. and Technol.) **14**, (1961) 69.
- [74] J. P. Butler, D. C. Santry, Canadian Journal of Chemistry, **39**, (1961) 689 .
- [75] D.M. Brink NUcl. Phys. **4**, 215 (1957); P. Axel, Phys. Rev. **126**, 671 (1962).
- [76] J.Kopecky, M. Uhl, and R.E. Chrien, Phys. Rev. C **47**, (1993) 312 .
- [77] M. Blann, *Phys. Rev. Lett.* **28** (1972) 757.
- [78] M. Blann, Code ALICE-91 PSR-146, *Statistical Model Code System with Fission Competition, Oak Ridge National Laboratory, Peripheral Shielding Routine Collection* (Livermore: Lawrence Livermore National Laboratory and IAEA) (1991).
- [79] Y. Ikeda, et al., JAERI Reports-1312 (1988) 1.
- [80] A. A. Filatenkov et al., Rept: Khlopin Radiev. Inst (1991) 252.
- [81] A. A. Filatenkov et al., Rept: Khlopin Radiev. Inst. (1999) 258.
- [82] M. M. Rahman, S. M. Qaim, Nucl. Phys. A **435** (1985) 43.
- [83] A. Marcinkowski, et al., Z. Phys. A **323** (1986) 91.
- [84] K. Xiangzhong et al., High Energy Phys. and Nucl. Phys. **15** (1991) 549 (Chinese ed).
- [85] T. D. Thiep et al., Nucl. Phys. A7 **22** (2003) 568c.
- [86] V. Semkova, R. Nolte, EPJ Web Conf. **66**, (2014) 03077.

- [87] S. Badwar et al., *Applied Radiation and Isotopes* 129 (2017) 117.
- [88] A. Gilbert, A.G.W. Cameron, *Can. J. Phys.* **43** (1965) 1446.
- [89] W. Dilg, W. Schantl, H. Vonach, M. Uhl, *Nucl. Phys. A* **217** (1973) 269.
- [90] A.V. Ignatyuk, K.K. Istekov, G.N. Smirenkin, *Sov. J. Nucl. Phys.* **29** 4 (1979) 450.
- [91] A.V. Ignatyuk, J.L. Weil, S. Raman, S. Kahane, *Phys. Rev. C* **47** (1993) 1504.
- [92] S. Goriely, S. Hilaire, A.J. Koning, *Improved microscopic nuclear level densities within the HFB plus combinatorial method*, *Phys. Rev. C* **78** (2008) 064307.
- [93] S. Hilaire, M. Girod, S. Goriely, A.J. Koning, *Temperature dependent combinatorial level densities with the D1M Gogny force, to be published* (2013).
- [94] B.S. Shivashankar, H. Naik, N. Sreekumaran Nair, S. Ganesan, S. V. Suryanarayana, K. Manjunatha Prasad, *Nucl. Sci. and Eng.*, **179**, (2015) 423. DOI: 10.13182/NSE14-19.
- [95] B.S. Shivashankar H. Naik, S.V. Suryanarayana, P.M. Prajapati, V.K. Mulik, K.C. Jagadeesan, S.V. Thakare, A. Goswami, S. Ganesan, *Jour. of Radioanalytical and Nuclear Chemistry*, **292**, (2012) 745. DOI: 10.1007/s10967-012-1646-9.
- [96] F. Zhou, Xiajie Xiao, Kaihong Fang, Changlin Lan, Xiangzhong Kong, *Nucl. Instrum. Methods in Physics Res. B*, **269** (2011) 642. DOI: 10.1016/j.nimb.2011.01.008
- [97] M. Bhike, A. Saxena, B.K. Nayak, S. Ganesan, B. Lalremruata, R. Palit, R. Tripathi, S. Sodaye, A.V.R. Reddy, S. Kailas, R.K. Choudhury, *conf. Nucl. Data for Adv. Nucl. Systems, Mangalore, India, 2006*, p.(TP15) (2006).
- [98] T. Shimizu, H. Sakane, M. Shibata, K. Kawade, T. Nishitani, *Annals of Nuclear Energy*, **31**, (2004) 975. DOI: 10.1016/j.anucene.2003.12.005
- [99] T. Senga, H. Sakane, M. Shibata, H. Yamamoto, K. Kawade, Y. Kasugai, Y. Ikeda, H. Takeuchi, T. Furuta *Japanese report to the I.N.D.C.*, No.185/U (2000)
- [100] Xiaolong Huang, Weixiang Yu, Xiaogang Han, Wenrong Zhao, Hanlin Lu, Jinxiang Chen, Zhaomin Shi, Gouyou Tang, Guohui Zhang, *Nuclear Science and Engineering*, **131**, (1999) 267. DOI: 10.13182/NSE99-A2033.

- [101] V. Avrigeanu, S. Sudar, Cs.M. Buczko, J. Csikai, A.A. Filatenkov, S.V. Chuvaev, R. Doczi, V. Semkova, V.A. Zelenetsky, *Physical Review C*, **60**, (1999) 017602. DOI: 10.1103/PhysRevC.60.017602.
- [102] J.C. Suita, A.G.da Silva, L.T. Auler, S.de Barros, *Nuclear Science and Engineering*, **126**, (1997) 101. DOI: 10.13182/NSE97-A24461
- [103] Cs.M. Buczko, J. Csikai, S. Sudar, A. Grallert, S.A. Jonah, B.W. Jimba, T. Chimoye, M. Wagner, *Physical Review C*, **52**, Issue.4, (1995) 1940. DOI: 10.1103/PhysRevC.52.1940.
- [104] I. Garlea, Chr. Miron-Garlea, H.N. Rosu, G. Fodor, V. Raducu, *Revue Roumaine de Physique*, **37**, Issue. 1, (1992) 19 .
- [105] M. Belgaid, M. Siad, M. Allab, *J. of Radioanalytical and Nucl. Chem., Letters*, **166**, Issue.6, (1992) 493. DOI: 10.1007/BF02163532.
- [106] Li Tingyan, Shi Zhaomin, Lu Hanlin, Zhao Wenrong, Yu Weixiang, Yuan Xialin, *High Energy Physics and Nucl. Physics, Chinese ed.*, **16**, Issue.2, (1992) 151.
- [107] L.I. Klochkova, B.S. Kovrigin, V.N. Kuritsin, Rept: USSR report to the I.N.D.C., No.376 (1994).
- [108] D.L. Smith, J.W. Meadows, H. Vonach, M. Wagner, R.C. Haight, W. Mannhart, *Conf. on Nucl.Data for Sci.and Technol.*, Juelich 1991, (1991) 282.
- [109] P.M. Dighe, G.R. Pansare, R. Sarkar, V.N. Bhoraskar, *Jour. of Physics G* **17**, (1991) L169. DOI: 10.1088/0954-3899/17/9/005.
- [110] H. Vonach, M. Wagner, R.C. Haight, *Nucl. En. Agency Nucl. Data Committee reports*, No.259, (1990) 165.
- [111] Y. Ikeda, C. Konno, K. Kosako, K. Oishi, *Japanese report to NEANDC*, No.155, (1990) 11.
- [112] A.A. Filatenkov, Rept: USSR report to the I.N.D.C., No.0460 (2016), <https://www-ds.iaea.org/publications/indc/indc-ccp-0460/>.
- [113] W. Mannhart, D. Schmidt, *Conf. on Nucl. Data for Sci. and Techn.*, Santa Fe 2004, **1**, (2004) 609. DOI: 10.1063/1.1945083.
- [114] A.K.M. Harun-Ar-Rashid, M.U. Khandaker, M.N. Islam, A.K.M.M.H. Meaze, Sk.A. Latif, M.A. Halim, K. Naher, M.N. Chowdhury, M.S. Uddin, M.A. Hafiz, M.M. Rahman, *Indian Journal of Physics*, **80**, (2006) 737.

- [115] Y. Uno, S. Meigo, S. Chiba, T. Fukahori, Y. Kasugai, O. Iwamoto, P. Siegler, Y. Ikeda, 9th Internat. Symposium on Reactor Dosimetry, Prague, (1996) 465.
- [116] S. Iwasaki, M. Sakuma, K. Sugiyama, N. Odano, JAERI-M Reports, No. 93-046, (1993) 257.
- [117] Yuan Junqian, Wang Yongchang, Kong Xiangzhong, Yang Jingkang , High Energy Physics and Nucl. Physics, Chinese ed., **16**, Issue.1, (1992) 57.
- [118] M. Viennot, M. Berrada, G. Paic, S. Joly, Nuclear Science and Engineering, **108**, (1991) 289. DOI: 10.13182/NSE87-157.
- [119] N.I. Molla, R.U. Miah, M. Rahman, Aysha Akhter, Conf.on Nucl.Data for Sci.and Technol.,Juelich 1991, (1991) 355.
- [120] I. Kimura, K. Kobayashi, Nuclear Science and Engineering, **106**, (1990) 332. DOI: 10.13182/NSE90-A29061.
- [121] Li Guozheng, Jiang Jinghe, High Energy Physics and Nucl. Physics, Chinese ed., **14**, Issue.11, (1990) 1023.
- [122] Y. Ikeda, C. Konno, K. Oishi, T. Nakamura, H. Miyade, K. Kawade, H. Yamamoto, T. Katoh, JAERI Reports, No.1312 (1988).
- [123] B. Champine, M.E. Gooden, Krishichayan, E.B. Norman, N.D. Scielzo, M.A. Stoyer, K.J. Thomas, A.P. Tonchev, W. Tornow, B.S. Wang, Physical Review C **93** (2016)014611, DOI:10.1103/PhysRevC.93.014611.
- [124] J. Vrzalova, O. Svoboda, A. Krasa, A. Kugler, M. Majerle, M. Suchopar, V. Wagner, Nucl. Instrum. Methods in Physics Res., Sect.A, **726**, (2013) 84. DOI:10.1016/j.nima.2013.05.133.
- [125] M.A. Hafiz, Indian Journal of Pure and Applied Physics, **45**, (2007) 425.
- [126] K.T. Osman, F.I. Habbani, Rept: Sudanese report to the I.N.D.C., No.001 (1996).
- [127] G.R. Pansare, V.N. Bhoraskar, Int. Journal of Modern Physics, Part E, **2**, Issue.01, (1993) 259, DOI: 10.1142/S021830139300008X.
- [128] M. Sakuma, S. Iwasaki, H. Shimada, N. Odano, K. Suda, J.R. Dumais, K. Sugiyama, JAERI-M Reports, No.92-027, (1992) 278.

- [129] A. Ercan, M.N. Erduran, M. Subasi, E. Gueltekin, G. Tarcan, A. Baykal, M. Bostan, Conf.on Nucl.Data for Sci.and Technol., Juelich 1991, (1991) 376.
- [130] Lu Hanlin, Huang Jianzhou, Fan Peiguo, Cui Yunfeng, Zhao Wenrong, Chinese report to the I.N.D.C., No.16 (1989).
- [131] A.S. Ilijinov et al., *Nucl. Phys. A* **534**, (1992) 517.
- [132] R. Capote, et al., *Nucl. Data Sheets* **110** (2009) 3107.
- [133] P.M. Gopych et al., Proceedings of the Conference Nucl. Spectr. and Structure of Atomic Nuclei, Kiev (1987) 533.
- [134] Y. Ikeda et al., Report JAERI-1312 (1988).
- [135] W.D. Lu et al., *Phys. Rev. C* **1** (1970) 350.
- [136] E. Betak et al., *Radiochim. Acta* **93**, (2005) 311.
- [137] Z. Zhong-Sheng et al., *Chin. Phys. C* **35**, (2011) 445.
- [138] W. Struve, G. Winkler, *Nucl. Phys. A* **222**, (1974) 605.
- [139] S.S. Hasan et al., *Nucl. Phys.* **181**, (1972) 101.
- [140] S. Lulic et al., *Nucl. Phys. A* **119**, (1968) 517.
- [141] J. Brzosko, P. Decowski, Z. Wilhelmi, *Nucl. Phys.* **45** (1963) 579.
- [142] J. Brzosko, P. Decowski, K. Siwek-Diamant, Z. Wilhelmi, *Nucl. Phys.* **74**, (1965) 438.
- [143] W. Grochalski, S. El-Konsol, A. Marcinkowski, *Acta Phys. Pol. B* **6**, (1975) 139.
- [144] A.P. Klyucharev, V.V. Ushakov, G.P. Chursin, *Zh. Eksp. Teor. Fiz.* **46**, (1964) 1483 (in Russian).